2013/09/12
Head Id: 203639
Archive Id: 206677:206728M
Archive Date: 2013/08/21
Archive Tag: trunk

Alignment of the CMS Tracker with Large Hadron Collider Data

The CMS Collaboration

Abstract

The central component of the CMS detector is the largest silicon tracker ever built. The precise alignment of this complex device is a formidable challenge, and only achievable with a significant extension of the technologies routinely used for tracking detectors in the past. This article describes the full-scale alignment procedure as it is used during LHC operations. Among the particular features of the method are the simultaneous determination of up to 200,000 alignment parameters with tracks, the measurement of individual sensor curvature parameters at the module level, the control of systematic misalignment effects, and the implementation in a multi-processor environment for fast execution speed.

Contents

1 Introduction

The scientific program of the Compact Muon Solenoid (CMS) experiment [1] at the Large Hadron Collider (LHC) [2] covers a very broad spectrum of physics and focuses on the search for new phenomena in the TeV range. Excellent tracking performance is crucial for reaching these scientific goals, which places very high demands on the level of precision of the calibration and alignment of the tracking devices. The task of the CMS tracker [3, 4] is to measure the trajectories of charged particles (tracks) with excellent momentum, angle, and position resolution, retaining high reconstruction efficiency [5]. According to design specifications, the tracking should reach a resolution on the transverse momentum, p_T, of 1.5% (10%) for muons of momentum of 100 (1000) GeV/c [5].

Misalignment of the tracker modules is a potentially limiting factor for its performance and should thus be reduced to the smallest possible levels. The large number of individual tracker modules, and their arrangement over a large volume, with some sensors as far as ≈ 6 m apart, take the alignment challenge to a new stage compared to earlier experiments. Because of the limited accessibility of the tracker inside CMS and the high level of precision required, the alignment technique is based on the tracks reconstructed by the tracker. Since the typical intrinsic hit resolution is between 10 and 30 μm [6, 7], the statistical accuracy of the alignment is targeted to stay significantly below these levels.

Another important aspect is the efficient control of any possible systematic biases in the alignment of the tracking modules, which might degrade the physics performance of the experiment. Systematic distortions of the aligned geometry could potentially be either introduced by biases in the hit and track reconstruction, inaccurate treatment of material effects and esti-

mation of the magnetic field, or by the lack of sensitivity of the alignment procedure itself to such degrees of freedom. Large samples of events with different track topologies are needed to identify and suppress such distortions, representing a particularly challenging aspect of the alignment effort.

The methodology of the tracker alignment at CMS builds on past experiences that were instrumental for the fast start-up of the tracking at the begining of LHC operations. Beyond simulation studies [8], the alignment at the Tracker Integration Facility (TIF) [9] proved the readiness of the alignment framework prior to the installation of the tracker in CMS by aligning a setup with approximately 15% of the silicon modules with cosmic ray tracks. Before the first proton-proton collisions at the LHC, cosmic muons were recorded by CMS in a dedicated run named Cosmic Run At Four Tesla (CRAFT) [10] with the magnetic field at the nominal value, which were used to align and calibrate the various subdetectors. The complete alignment of the tracker with the CRAFT data involved 3.2 million of cosmic ray tracks passing stringent quality requirements, as well as optical survey measurements done before the final installation of the tracker [11]. The alignment achieved a statistical precision of 3-4 μm and 3-14 μm in the barrel and endcap regions, respectively. The performance of the tracking at CMS has been studied during the first period of proton-proton collisions at the LHC and proved to be very good already at the start of the operations [12, 13].

While the alignment obtained from CRAFT was instrumental for the early physics program of CMS, its quality was still limited statistically by the available number of cosmic ray tracks, mainly in the pixel endcaps, and systematically by the kinematic diversity in the track sample. Achievement of the ultimate accuracy requires inclusion of the large statistics of tracks from proton-proton collisions provided by the LHC. This article describes the full alignment procedure for the modules of the CMS tracker and the validation of the obtained geometry. The procedure uses tracks from cosmic ray muons and proton-proton collisions recorded in 2011. Its result has been used for the reprocessing of the 2011 data and the start of the 2012 data taking. A similar procedure has later been applied to 2012 data, which is beyond the scope of this article.

2 Tracker layout and coordinate system

The CMS experiment uses a right-handed coordinate system, with the origin at the nominal collision point, the x-axis pointing to the centre of the LHC, the y-axis pointing up (perpendicular to the LHC plane), and the z-axis along the anticlockwise-beam direction. The polar angle (θ) is measured from the positive z-axis and the azimuthal angle (φ) is measured from the positive x-axis in the $x-y$ plane, whereas the radius (r) denotes the distance from the z-axis. The pseudorapidity, η, is defined as $\eta = -\ln[\tan(\theta/2)]$.

A detailed description of the CMS detector can be found in Ref. [1]. The central feature of the CMS detector is a 3.8 T superconducting solenoid of 6 m internal diameter. Within the inner field volume, starting from the smallest radius, reside the silicon tracker, the crystal electromagnetic calorimeter (ECAL), and the brass-scintillator hadron calorimeter (HCAL). The muon system is installed outside of the solenoid, embedded in the steel return yoke.

The CMS tracker is composed of 1440 silicon pixel and 15 148 silicon microstrip modules organised in six sub-assemblies, as shown in Figure 1. Pixel modules of the CMS tracker are grouped into the barrel pixel (BPIX) and the forward pixel (FPIX) in the endcap regions. Strip modules in the central pseudorapidity region are divided into the Tracker Inner Barrel (TIB) at smaller and the Tracker Outer Barrel (TOB) at larger radii. Similarly strip modules in the endcap re-

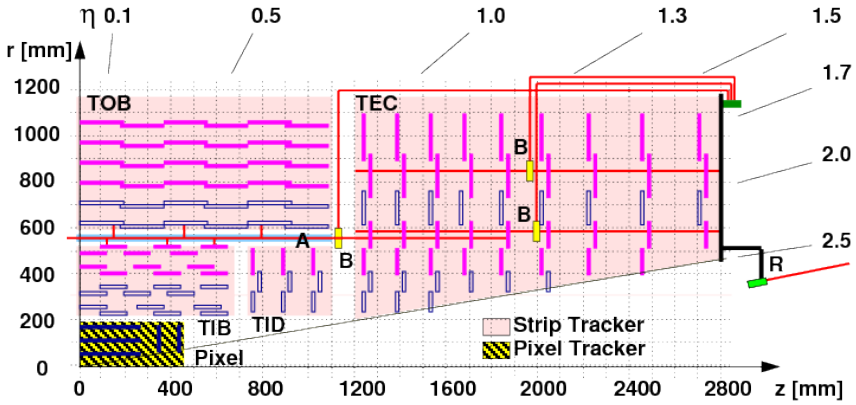

Figure 1: Schematic view in the rz plane of a quarter of the silicon tracker. The positions of the pixel modules are indicated within the hatched area. At larger radii within the lightly shaded areas, solid rectangles represent single strip modules, while hollow rectangles indicate pairs of strip modules with a relative stereo angle mounted back-to-back. The figure illustrates also the paths of the laser rays (R), the alignment tubes (A) and the beam splitters (B) of the Laser Alignment System.

gions are arranged in a Tracker Inner Disk (TID) and Tracker Endcaps (TEC) at smaller and larger z coordinates, respectively.

The BPIX system is divided into two semi-cylindrical half-shells along the $y-z$ plane. TIB and TOB are both divided into two half-barrels at positive and negative z, respectively. The pixel modules composing the BPIX half-shells are mechanically assembled in three concentrical layers. Similarly, four and six layers of microstrip modules compose the TIB and TOB half-barrels, respectively. FPIX, TID and TEC are all divided in two symmetrical parts in the forward ($z > 0$) and backward ($z < 0$) region. Each of these halves is composed of a series of disks arranged at different z; there are two, three and nine of such disks for FPIX, TID and TEC, respectively. Each FPIX disk is subdivided into two mechanically independent half-disks. The modules on the TID and TEC disks are further arranged in concentrical rings numbered from 1 (innermost) to 3 (outermost) in TID and from 1 to 7 in TEC.

Pixel modules provide a bidimensional measurement of the hit position. Strip modules in the barrel (endcap) generally measure the global $r\varphi$ (φ) coordinate of the hit. The two layers of TIB and TOB at smaller radii, rings 1 and 2 in TID and rings 1, 2 and 5 in TEC are instrumented with pairs of microstrip modules mounted back-to-back, referred to as "$r\varphi$" and "stereo" modules, respectively. The strip direction of the stereo modules is tilted by 100 mrad relative to that of the "$r\varphi$" modules, which allows inferring a measurement in the z-direction in the barrel and in the r-direction in the endcaps. The modules in the TOB and in rings 5-7 of the TEC consist of pairs of sensors with strips connected in series.

The strip modules have the possibility to take data in two different configurations, called peak and deconvolution modes [14, 15]. The peak mode uses directly the signals from the analogue pipeline, which stores the amplified and shaped signals every 25 ns. In the deconvolution mode, a weighted sum of three consecutive samples is formed, which effectively reduces the rise time and contains the whole signal in 25 ns. The peak mode is characterised by a better signal-over-noise ratio and a longer integration time, ideal for collecting cosmic ray tracks that appear at random times, but not suitable for the high bunch crossing frequency of the LHC. Therefore, the strip tracker is operated in deconvolution mode when recording data during LHC operation.

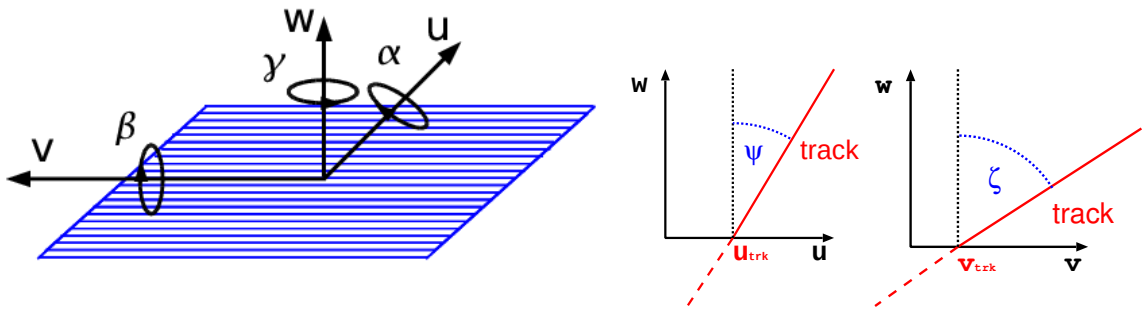

Figure 2: Sketch of a silicon strip module showing axes of its local coordinate system, u, v and w, the respective local rotations α, β, γ (left) and illustrations of the local track angles ψ and ζ (right)

A local right-handed coordinate system is defined for each module with the origin at the geometric centre of the active area of the module. As illustrated in the left of Figure 2, the u-axis is defined along the more precisely measured coordinate of the module (typically along the azimuthal direction in the global system), the v-axis orthogonal to the u-axis and in the module plane, pointing away from the readout electronics, and the w-axis normal to the module plane. The origin of the w axis is in the middle of the module thickness. For the pixel system, u is chosen orthogonal to the magnetic field, i.e. in global $r\varphi$ direction in the BPIX and in the radial direction in the FPIX. The v coordinate is perpendicular to u in the sensor plane, i.e. along global z in the BPIX and at a small angle to the global $r\varphi$ direction in the FPIX. The angles α, β, and γ indicate right-handed rotations about the u, v, and w axes, respectively. As illustrated in the right of Figure 2, the local track angle ψ (ζ) with respect to the module normal is defined in the uw (vw) plane.

3 Global position and orientation of the tracker

While the track-based internal alignment (see Section 4) mainly adjusts the positions and angles of the tracker modules relative to each other, it cannot ascertain the absolute position and orientation of the tracker. Survey measurements of the TOB, as the largest single subcomponent, are thus used to determine its shift and rotation around the beam axis, relative to the design values. The other subcomponents are then aligned relative to the TOB using the track-based internal alignment procedure. The orientation of the tracker relative to the magnetic field is of special importance, since the correct parameterization of the trajectory in the reconstruction depends on it. This global orientation is described by the angles θ_x and θ_y, which correspond to rotations of the whole tracker around the x and y axes defined in the previous section. Uncorrected overall tilts of the tracker relative to the magnetic field could result in biases of the reconstructed parameters of the tracks and the visible masses of resonances inferred from their charged daughter particles. Such biases would be hard to disentangle from other systematic effects as they will be addressed in Section 4.4. It is therefore essential to determine the global tracker tilt angles and include these in the overall alignment correction. It is not expected that tilt angles will change significantly with time, hence one measurement should be sufficient for many years of operation. The tilt angles have been determined with the 2010 CMS data, and they have been used as input for the internal alignment detailed in subsequent sections of this article. A repetition of the procedure with 2011 data is found to show compatible results.

The measurement of the tilt angles is based on the study of overall track quality under variation

of the θ_x and θ_y angles. Any non-optimal setting of the tilt angles will result e.g. in incorrect assumptions concerning the transverse field components relative to the tracker axis that degrade the observed track quality. The tilt angles θ_x and θ_y are scanned. For each set of values, the standard CMS track fit is applied to the whole set of tracks, and an overall track quality estimator is determined. Three overall track quality estimators are studied:

- the mean normalised track χ^2 per degree of freedom, $\langle \chi^2/\mathrm{N_{dof}} \rangle$, taken over all selected tracks,
- the mean χ^2 probability of the fit, $\langle \mathrm{Prob}(\chi^2, \mathrm{N_{dof}}) \rangle$,
- the total chi-square, $\sum \chi^2$.

Events are considered if they have exactly one primary vertex reconstructed using at least four tracks, and a reconstructed position along the beam line within ± 24 cm of the nominal centre of the CMS detector. Tracks are required to have at least ten reconstructed hits and a pseudorapidity of $|\eta| < 2.5$. The track impact parameter with respect to the primary vertex must be less than 0.15 cm in the transverse and less than 2 cm in the longitudinal direction. For the baseline analysis that provides the central values, the transverse momentum threshold is set to 1 GeV/c; alternative values of 0.5 and 2 GeV/c are used to study the systematic uncertainty. Only tracks with $\chi^2/\mathrm{N_{dof}} < 4$ are selected in order to reject those with wrongly associated hits. For each setting of the tilt angles, each track is refitted using a full 3D field model [16, 17] that also takes tangential field components into account. This field model is based on measurements obtained during a dedicated mapping campaign with Hall and NMR probes [18].

Each tilt angle is scanned at eleven settings in the range ± 2 mrad. The angle of correct alignment is derived as the point of optimum determined by a least squares fit with a second order polynomial function. The dependence of the mean χ^2 probability quality estimator on the tilt angles θ_x and θ_y is shown in Figure 3.

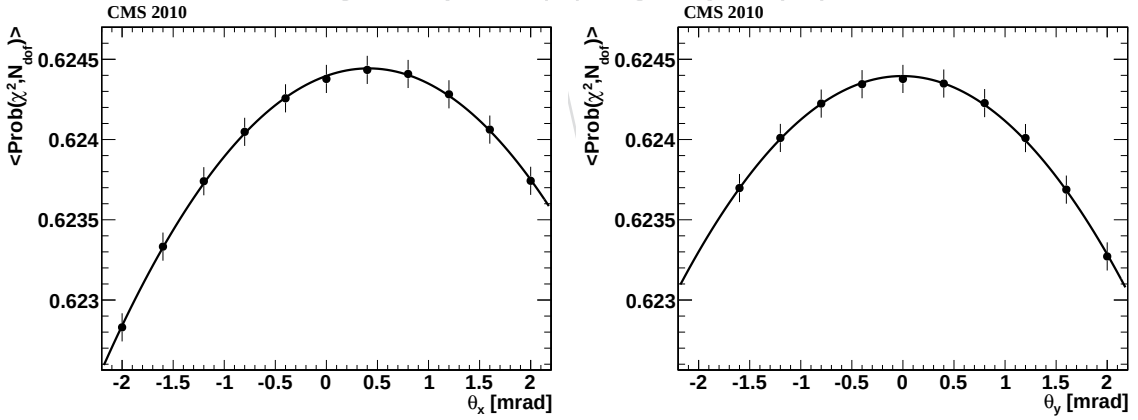

Figure 3: Dependence of the mean χ^2 probability of the track fit on the assumed θ_x (left) and θ_y rotation angles for $|\eta| < 2.5$. The optimum of track quality is obtained at $\theta_x \approx 0.3$ mrad and $\theta_y \approx 0$. Uncertainty bands reported for each values are statistical only and thus highly correlated among them.

In each plot, only one angle is varied, while the other remains fixed at 0. The second order polynomial fit describes the functional dependence very well. There is no result for the scan point at $\theta_y = -2$ mrad, because this setting is outside the tolerance of the track reconstruction framework. While the θ_y dependence is symmetric with a maximum near $\theta_y \approx 0$, the θ_x dependence peaks at about 0.3 mrad, indicating a noticeable vertical downward tilt of the tracker

around the x axis with respect to the magnetic field. On an absolute scale, the tilt is small, although well within the resolution of beam line tilt measurements [12]. Its effect on the mean track fit χ^2 probability is < 0.0002.

The straightforward statistical uncertainty estimation delivered by this fit is not directly usable, since each scan point uses the same tracks, which leads to a strong correlation of all points. Thus the determination of the statistical uncertainty is achieved with other methods depending on the respective quality estimator. For the mean normalised χ^2 and the mean χ^2 probability estimators, the track sample is divided into five subsamples, and the procedure is repeated. The statistical uncertainty is estimated from the standard deviation of the fit results. For the total χ^2 estimator, the statistical uncertainty margin is bounded by the parameter values with $\Delta\chi^2 = 1$ with respect to the minimum. All methods yield similar results; remaining small differences are attributed to the different relative weight of tracks with varying number of hits and the effect of any remaining outliers.

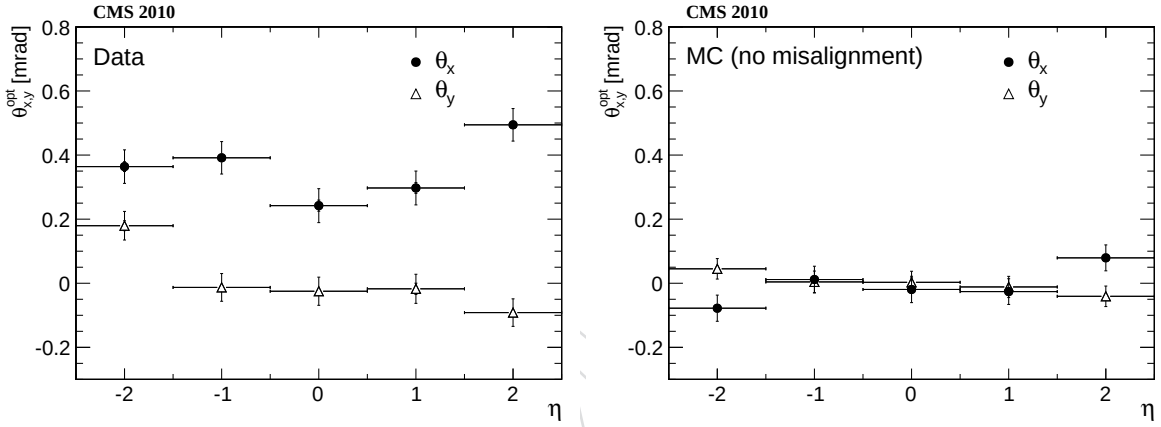

Figure 4: Visible tracker tilt angles θ_x (filled circles) and θ_y (hollow triangles) as a function of track pseudorapidity. The left plot shows the values measured with the data collected in 2010, the right plot has been obtained from simulated events without tracker misalignment. The statistical uncertainty is hardly larger than the symbol size and mostly invisible. The systematic uncertainty has be obtained from varying several parameters of the tilt angle determination (see text).

Figure 4 (left) shows the results for five intervals of track pseudorapidity, for tracks with $p_T > 1\,\text{GeV}/c$. The results obtained with the three track quality estimators and the corresponding statistical uncertainties have been averaged. The statistical uncertainties are at most of the order of the symbol size and thus hardly visible. The error bars are dominated by the systematic uncertainties, which are estimated as the RMS of the changes observed in the tilt angle estimates across the three track quality estimators used, and under the variation of the p_T cut. This systematic error estimate is averaged over the pseudorapidity intervals to mitigate statistical fluctuations. The measured tilt angles show variations of the order of ± 0.15 mrad as a function of pseudorapidity, which could point to subtle fine structures in the internal alignment of the detector, but are largely absorbed by the estimated systematic uncertainty.

As a cross-check, the method is also applied to simulated events without any tracker misalignment. The results are shown in Figure 4 (right). They are consistent with zero tilt within the systematic uncertainty. The variations are smaller in the central region within $|\eta| < 1.5$, and they are well contained within a margin of ± 0.1 mrad. For this reason, the nominal tilt angle values used as alignment constants are extracted from the central region of Figure 4 (left) and

set to $\theta_x = (0.3 \pm 0.1)$ mrad and $\theta_y = (0 \pm 0.1)$ mrad, thus eliminating an important potential source of systematic alignment uncertainty. These results represent an important complementary step to the internal alignment procedure described in the following sections.

4 Methodology of track-based internal alignment

Track-hit residual distributions are generally broadened if the assumed positions of the silicon modules used in track reconstruction differ from the true positions. Therefore standard alignment algorithms follow the least squares approach and minimise the sum of squares of normalised residuals from many tracks. Assuming the measurements m_{ij} with uncertainties σ_{ij} are independent, the minimised objective function is

$$\chi^2(\mathbf{p},\mathbf{q}) = \sum_{j}^{\text{tracks}} \sum_{i}^{\text{measurements}} \left(\frac{m_{ij} - f_{ij}\left(\mathbf{p},\mathbf{q}_j\right)}{\sigma_{ij}} \right)^2, \tag{1}$$

where f_{ij} is the trajectory prediction of the track model at the position of the measurement, depending on the geometry ($\mathbf{p}$) and track ($\mathbf{q}_j$) parameters. An initial geometry description $\mathbf{p}_0$ is usually available from design drawings, survey measurements, or previous alignment results. This can be used to determine approximate track parameters $\mathbf{q}_{j0}$. Since alignment corrections can be assumed to be small, f_{ij} can be linearised around these initial values. Minimising χ^2 after the linearisation leads to the normal equations of least squares. These can be expressed as a linear equation system $\mathbf{Ca} = \mathbf{b}$ with $\mathbf{a}^T = (\mathbf{\Delta p}, \mathbf{\Delta q})$, i.e. the alignment parameters $\mathbf{\Delta p}$ and corrections to all parameters of all n used tracks $\mathbf{\Delta q}^T = (\mathbf{\Delta q}_1, \ldots, \mathbf{\Delta q}_n)$. If the alignment corrections are not small, the linear approximation is of limited precision and the procedure has to be iterated.

For alignment of the CMS tracker a global fit approach [19] is applied, using the MILLEPEDE II program [20]. It makes use of the special structure of $\mathbf{C}$ that facilitates, using block matrix algebra, the reduction of the large system of equations $\mathbf{Ca} = \mathbf{b}$ to a smaller one for the alignment parameters only,

$$\mathbf{C}'\mathbf{\Delta p} = \mathbf{b}'. \tag{2}$$

$\mathbf{C}'$ and $\mathbf{b}'$ sum contributions from all tracks. To accumulate $\mathbf{b}'$, for each track a matrix equation $\mathbf{C}_j\mathbf{\Delta q}_j = \mathbf{b}_j$ has to be solved. For $\mathbf{C}'$, in addition $\mathbf{C}_j^{-1}$ needs to be calculated. The reduction of the matrix size from $\mathbf{C}'$ to $\mathbf{C}$ is dramatic. For 10^7 tracks with on average 20 parameters and 10^5 alignment parameters, the number of matrix elements is reduced by a factor above $4 \cdot 10^6$. Nevertheless, no information is lost for the determination of the alignment parameters $\mathbf{\Delta p}$.

The following subsections explain the track and alignment parameters $\mathbf{\Delta q}$ and $\mathbf{\Delta p}$ that are used for the CMS tracker alignment. Then the concept of a hierarchical and differential alignment using equality constraints is introduced, followed by a discussion of "weak modes" and how they can be avoided. The section closes with the computing optimisations needed to make MILLEPEDE II a fast tool with modest computer memory needs even for the alignment of the CMS tracker with its unprecented complexity.

4.1 Track parametrisation

In the absence of material effects, five parameters are needed to describe the trajectory of a charged particle in a magnetic field. Traversing material, the particle experiences multiple scattering, mainly due to Coulomb interaction with the electrons in the atoms. These effects are of

relevant size in the CMS tracker, i.e. the particle trajectory cannot be well described without taking them into account in the track model. This is now achieved in a rigorous and efficient way as explained in the following, an improvement compared to previous MILLEPEDE II alignment procedures [8, 9, 11] for the CMS silicon tracker.

A rigorous treatment of multiple scattering can be achieved by increasing the number of track parameters to $n_{par} = 5 + 2n_{scat}$, e.g. adding two deflection angles for each of the n_{scat} thin scatterers[1] traversed by the particle. Precise description of the tracker material distribution and preliminary knowledge of the particle momentum allow the estimation of the spread of the deflection angles. This spread is used as the precision of a virtual measurement of the deflection angle of null average value. For each scatterer, the list of measurements, originally containing all the track hits, is extended by two such virtual measurements. For cosmic ray tracks this complete parametrisation often leads to $n_{par} > 50$. Since in the general case the effort to calculate $\mathbf{C}_j^{-1}$ is proportional to n_{par}^3, a significant amount of computing time would be spent to calculate $\mathbf{C}_j^{-1}$ and thus $\mathbf{C}'$ and $\mathbf{b}'$. The progressive Kalman filter fit as used in the CMS track reconstruction [21] avoids the n_{par}^3 scaling by a sequential fit procedure, determining five track parameters at each measurement. But it does not provide the full (singular) covariance matrix $\mathbf{C}_j^{-1}$ of these parameters as needed in a global fit alignment approach. As shown in [22], the Kalman filter fit procedure can be extended to provide this covariance matrix, but since MILLEPEDE II is designed for a simultaneous fit of all measurements, another approach is followed here.

The General Broken Lines track refit [23, 24], based on [25], avoids the n_{par}^3 scaling for calculating $\mathbf{C}_j^{-1}$ by defining a custom track parametrisation. The parameters are $\mathbf{q}_j = (\Delta\frac{q}{p}, \mathbf{u}_1, \ldots, \mathbf{u}_{(n_{scat}+2)})$, where $\Delta\frac{q}{p}$ is the change of the inverse momentum multiplied by the particle charge and $\mathbf{u}_i$ are the two-dimensional offsets to an initial reference trajectory in local systems at each scatterer and at the first and last measurement. All parameters except $\Delta\frac{q}{p}$ influence only a small part of the track trajectory. This locality of all track parameters (but one) results in $\mathbf{C}_j$ being a bordered band matrix with band width $m \leq 5$ and border size $b = 1$, i.e. the matrix elements $c_{j,kl}$ are non-zero only for $k \leq b$, $l \leq b$ or $|k - l| \leq m$. Using root free Cholesky decomposition ($\mathbf{C}_j^{\text{band}} = \mathbf{L}\mathbf{D}\mathbf{L}^T$) of the band part $\mathbf{C}_j^{\text{band}}$ into a diagonal matrix $\mathbf{D}$ and a unit left triangular band matrix $\mathbf{L}$, the effort to calculate $\mathbf{C}_j^{-1}$ and $\mathbf{q}_j$ is reduced to $\propto n_{par}^2 \cdot (m + b)$ and $\propto n_{par} \cdot (m + b)^2$, respectively. This approach saves in CPU time in MILLEPEDE II a factor of 6.5 for isolated muons and 8.4 for cosmic ray tracks in comparison with an (equivalent) linear equation system with a full/non-sparse matrix solved by inversion [23].

The implementation of the General Broken Lines refit used for MILLEPEDE II alignment of the CMS tracker is based on a seed trajectory derived from the position and direction of the track at its first hit as resulting from the standard Kalman filter track fit. From the first hit, the trajectory is propagated taking into account magnetic field inhomogeneities (using the Runge-Kutta technique as described in [21]) and average energy loss in the material as for muons. As in the CMS Kalman track fit, all traversed material is assumed to coincide with the silicon measurement planes that are treated as thin scatterers. The curvilinear frame is chosen for the local coordinate systems at these scatterers. Parameter propagation along the trajectory needed to link the local systems uses Jacobians assuming a locally constant magnetic field between them [26]. To further reduce the computing time, two approximations are applied in the standard processing: material assigned to stereo and $r\varphi$ modules that are mounted together

[1] For thin scatterers, the trajectory offsets induced by multiple scattering can be ignored. If a scatterer is thick, it can be approximately treated as two thin scatterers.

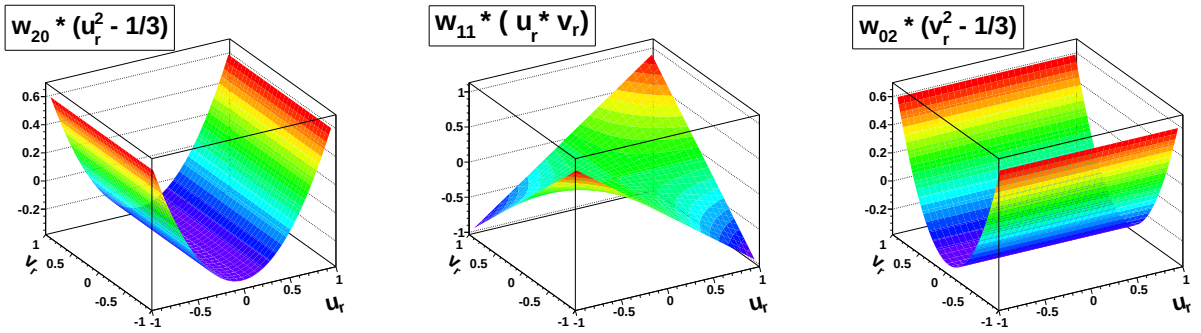

Figure 5: The three second order polynomials to describe sensor deviations from the flat plane.

is treated as a single thin scatterer, and the Jacobians are calculated assuming the magnetic field $\vec{B}$ to be parallel to the z-axis and in the limit of weak deflection, $\frac{|\vec{B}|}{p} \to 0$. This leads to a band width of $m = 4$.

4.2 Alignment parametrisation

To first approximation, the CMS silicon modules are flat planes. Thus previous alignment approaches in CMS determined corrections to the initial module positions, i.e. up to three shifts (u, v, w) and three rotations (α, β, γ), see Figure 2. Tracks with large angles of incidence relative to the silicon module normal are highly sensitive to the exact positions of the modules in their w directions and therefore also to local w variations if the modules are not flat. These local variations can arise from silicon sensors being curved and, for strip modules with two sensors in a chain, from their relative misalignment. In fact, sensor curvatures can be expected due to single sided silicon processing. For strip sensors, the specification for construction has been less than 100 μm deviation [1] from being flat. To take into account that modules are not flat, the vector of alignment parameters $\mathbf{\Delta p}$ is extended to up to nine degrees of freedom per sensor instead of six per module. The sensor shape is parametrised as a sum of products of modified (orthogonal) Legendre polynomials up to the second order where the constant and linear terms are equivalent to the rigid body parameters w, α and β:

$$\begin{aligned} w(u_r, v_r) = \quad & w \\ & + w_{10} \cdot u_r && + w_{01} \cdot v_r \\ & + w_{20} \cdot (u_r^2 - 1/3) && + w_{11} \cdot (u_r \cdot v_r) \quad + w_{02} \cdot (v_r^2 - 1/3). \end{aligned} \tag{3}$$

Here $u_r \in [-1, 1]$ ($v_r \in [-1, 1]$) is the position on the sensor in the u- (v-) direction, normalised to its width l_u (length l_v). The coefficients w_{20}, w_{11} and w_{02} describe the amplitude of the sensor curvature as illustrated in Figure 5.

To linearise the track model prediction f_{ij}, derivatives with respect to the alignment parameters have to be calculated. The derivatives for the predictions f_u and f_v in the directions of the local

coordinates u and v are

$$\begin{pmatrix} \frac{\partial f_u}{\partial u} & \frac{\partial f_v}{\partial u} \\ \frac{\partial f_u}{\partial v} & \frac{\partial f_v}{\partial v} \\ \frac{\partial f_u}{\partial w} & \frac{\partial f_v}{\partial w} \\ \frac{\partial f_u}{\partial w_{10}} & \frac{\partial f_v}{\partial w_{10}} \\ \frac{\partial f_u}{\partial w_{01}} & \frac{\partial f_v}{\partial w_{01}} \\ \frac{\partial f_u}{\partial \gamma'} & \frac{\partial f_v}{\partial \gamma'} \\ \frac{\partial f_u}{\partial w_{20}} & \frac{\partial f_v}{\partial w_{20}} \\ \frac{\partial f_u}{\partial w_{11}} & \frac{\partial f_v}{\partial w_{11}} \\ \frac{\partial f_u}{\partial w_{02}} & \frac{\partial f_v}{\partial w_{02}} \end{pmatrix} = \begin{pmatrix} -1 & 0 \\ 0 & -1 \\ \tan\psi & \tan\zeta \\ u_r \cdot \tan\psi & u_r \cdot \tan\zeta \\ v_r \cdot \tan\psi & v_r \cdot \tan\zeta \\ v_r l_v/(2\,s) & -u_r l_u/(2\,s) \\ (u_r^2 - 1/3) \cdot \tan\psi & (u_r^2 - 1/3) \cdot \tan\zeta \\ u_r \cdot v_r \cdot \tan\psi & u_r \cdot v_r \cdot \tan\zeta \\ (v_r^2 - 1/3) \cdot \tan\psi & (v_r^2 - 1/3) \cdot \tan\zeta \end{pmatrix}. \tag{4}$$

Here the track angle from the sensor normal ψ (ζ) is defined in the uw (vw) plane (Figure 2) and the track predictions are used for u_r and v_r.

Different from the parametrisation used in previous CMS alignment procedures [27], the coefficients of the first order polynomials $w_{01} = \frac{l_v}{2} \cdot \tan\alpha$ and $w_{10} = \frac{-l_u}{2} \cdot \tan\beta$ are used as alignment parameters instead of the angles. This ensures the orthogonality of the sensor surface parametrisation. The in-plane rotation γ is replaced by $\gamma' = s \cdot \gamma$ with $s = \frac{l_u + l_v}{2}$. This has the advantage that all parameters have a length scale and their derivatives similar numerical size.

The pixel modules provide uncorrelated measurements in both u and v directions. The strips of the modules in the TIB and TOB are parallel along v, so the modules provide measurements only in the u direction. For TID and TEC modules, where the strips are not parallel, the hit reconstruction provides highly correlated two-dimensional measurements in u and v. Their covariance matrix is diagonalised and the corresponding transformation applied to the derivatives and residuals as well. The measurement in the less precise direction, after the diagonalisation, is skipped.

4.3 Hierarchical and differential alignment using equality constraints

The CMS tracker is built in a hierarchical way from mechanical substructures, e.g. three BPIX layers form each of the two BPIX half-shells. To treat translations and rotations of these substructures as a whole, six alignment parameters $\mathbf{\Delta p}_l$ for each of the considered substructures can be introduced. The derivatives of the track prediction with respect to these parameters, $df_{u/v}/d\mathbf{\Delta p}_l$, are obtained from the six translational and rotational parameters of the hit sensor $\mathbf{\Delta p}_s$ by coordinate transformation using the chain rule,

$$\frac{df_{u/v}}{d\mathbf{\Delta p}_l} = \frac{d\mathbf{\Delta p}_s}{d\mathbf{\Delta p}_l} \cdot \frac{df_{u/v}}{d\mathbf{\Delta p}_s}, \tag{5}$$

where $\frac{d\mathbf{\Delta p}_s}{d\mathbf{\Delta p}_l}$ is the 6x6 Jacobian matrix expressing the effect of translations and rotations of the large structure on the position of the sensor.

These large substructure parameters are useful in two different cases. The first is the correction for misplacements of these substructures with e.g. limited statistics. In addition they can be used in a hierarchical alignment approach, simultaneously with the alignment parameters of the sensors. This has the advantage that coherent misplacements of large structures in directions of the non-sensitive coordinate v of strip sensors can be taken into account.

This hierarchical approach introduces redundant degrees of freedom. They are eliminated using linear equality constraints. In general, these constraints can be formulated as

$$\sum_i c_i \, \Delta p_i = s \tag{6}$$

where the index i runs on all alignment parameters. In MILLEPEDE II these constraints are implemented by extending the matrix Equation (2) using Lagrangian multipliers. In the hierarchical approach, for each parameter Δp_l of the larger structure one constraint with $s = 0$ has to be applied and then all constraints for one large structure form a matrix equation,

$$\sum_{i \in components} \left[\frac{d\mathbf{\Delta p}_{s,i}}{d\mathbf{\Delta p}_l} \right]^{-1} \cdot \mathbf{\Delta p}_i = \mathbf{0}, \tag{7}$$

where $\mathbf{\Delta p}_{s,i}$ are the shift and rotation parameters of component i of the large substructure. Similarly, the technique of equality constraints is used to fix the six undefined overall shifts and rotations of the complete tracker.

The concept of "differential alignment" means that some parameters are defined as variable across the input dataset, while the bulk of the parameters is treated to be constant. This method allows the use of the full statistical power of the whole dataset for the determination of parameters that are stable with time, without neglecting the time dependence of others. This is especially useful in conjunction with a hierarchical alignment: The parameters of larger structures can vary with time, but the sensors therein are kept stable relative to their large structure, as is enforced by the constraints to eliminate the redundant degrees of freedom.

4.4 Weak modes

A major difficulty of track-based alignment arises if the matrix $\mathbf{C}'$ in Equation (2) is ill-conditioned, i.e. singular or numerically close to singular. This is due to linear combinations of the alignment parameters that do not (or only slightly) change the track-hit residuals and thus the overall $\chi^2(\mathbf{\Delta p}, \mathbf{\Delta q})$ in Equation (1), after linearisation of the track model f_{ij}. These linear combinations are called "weak modes" since the amplitudes of their contributions to the solution are barely determinable – if at all.

Weak modes can emerge if certain coherent changes of alignment parameters $\mathbf{\Delta p}$ can be compensated by changes of the track parameters $\mathbf{\Delta q}$. The simplest example is an overall shift of the tracker that would be compensated by changes of the impact parameters of the tracks. For that reason the overall shift has to be fixed using constraints as mentioned above. A particular problem is that even very small biases in the track model f_{ij} can lead to a significant distortion of the tracker if the equivalent linear combination of the alignment parameters is not well determined by the data fed into Equation (1). As a result, weak modes contribute siginificantly to the systematic uncertainty of kinematic properties determined from the track fit.

The scope of possible weak modes depends largely on the geometry and segmentation of the detector, the topology of the tracks used for alignment, and on the alignment and track parameters. The CMS tracker has a highly segmented detector geometry with a cylindrical layout within a solenoidal magnetic field. If aligned only with tracks passing through the beam line, the characteristic weak modes can be classified in cylindrical coordinates, i.e. by module displacements Δr, Δz and $\Delta\phi$ as functions of r, z and ϕ [28]. To control these weak modes it is crucial to include additional information in Equation (1), e.g. by combining track sets of different topological variety and from physics constraints, using

- cosmic ray tracks that break the cylindrical symmetry,
- straight tracks without curvatures, recorded when the magnetic field is off,
- knowledge about the production vertex of tracks,
- knowledge about the invariant mass of a resonance whose decay particles are observed as tracks.

Earlier alignment studies [11] have shown that the usage of cosmic ray tracks is quite effective in controlling several classes of weak modes. However, for some types of coherent deformations of the tracker the sensitivity of an alignment using cosmic ray tracks is limited. A prominent example biasing the track curvature $\kappa \propto \frac{q}{p_\mathrm{T}}$ (with q being the track charge) is a *twist* deformation of the tracker, in which the modules are moved coherently in ϕ by an amount directly proportional to their longitudinal position ($\Delta\varphi = \tau \cdot z$). This has been studied extensively in [29]. Other potential weak modes are the off-centring of the barrel layers and endcap rings (*sagitta*), described by $(\Delta x, \Delta y) = \sigma \cdot r \cdot (\sin\varphi_\sigma, \cos\varphi_\sigma)$, and a *skew*, parametrised as $\Delta z = \omega \cdot \sin\varphi_\omega$. Here σ and ω denote the amplitudes of the weak modes whereas φ_σ and φ_ω are their azimuthal phases.

As a measure against weak modes that influence the track momenta, such as a twist deformation, information about the mass of a resonance decaying into two charged particles is included in the alignment fit with the following method. A common parametrisation for the two trajectories of the particles produced in the decay is defined in [30]. Instead of 2×5 parameters (plus those accounting for multiple scattering), the nine common parameters are the position of the decay vertex, the momentum of the resonance candidate, two angles defining the direction of the decay products in the rest-frame of the resonance, and the mass of the resonance. The mass of the resonance is added as a virtual measurement with an uncertainty corresponding to the standard deviation of the resonance line shape around the peak position, as observable after final state radiation. In the sum on the right hand side of Equation (1), the two individual tracks are replaced by the common fit object. With the broken lines parametrisation the corresponding $\mathbf{C}_j$ has the border size $b = 9$. This approach to include resonance mass information in the alignment fit implies an implementation of a vertex constraint as well, since the coordinates of the decay vertex are parameters of the combined fit object and thus force the tracks to a common vertex.

The dependence of the reconstructed resonance mass M on the size τ of a twist deformation can be shown to follow

$$\frac{\partial M^2}{\partial \tau} = \left(\frac{M^2}{p^+} \frac{\partial p^+}{\partial \tau} + \frac{M^2}{p^-} \frac{\partial p^-}{\partial \tau} \right) = \frac{2M^2}{B_z} \left(p_z^+ - p_z^- \right). \tag{8}$$

Here B_z denotes the strength of the solenoidal magnetic field along the z-axis, p^+ (p^-) and p_z^+ (p_z^-) are the momentum and its longitudinal component of the positively (negatively) charged particle, respectively. The equation shows that the inclusion of a heavy resonance such as the Z^0 boson in the alignment procedure is more effective for controlling the twist than the J/ψ and Y quarkonia, since at the LHC the decay products of the latter are usually boosted within a narrow cone, and the difference of their longitudinal momenta is small. The decay channel of Z^0 to muons is particularly useful because the high-p_T muons are measured precisely and with high efficiency by the CMS detector. The properties of the Z^0 boson are predicted by the Standard Model and have been characterised experimentally very well at the LHC [31, 32] and in past experiments [33]. This allows using the muonic decay of the Z^0 as a standard candle both for adding to the alignment procedure sensitivity against systematic distortions and for verifying the absence of any bias on the track reconstruction.

Under certain conditions equality constraints can be utilised against a weak mode. Its corresponding linear combination of alignment parameters has to be known together with the amplitude of the distortion in the starting geometry. If e.g. each aligned object i of the starting geometry is systematically misplaced in φ according to a twist τ with reference point z_0 ($\Delta\varphi_i = \tau \cdot (z_i - z_0)$), as known from an external reference, a constraint can be used in a further alignment step to compensate for this effect. This constraint takes the form $\sum_i \sum_j \Delta p_{ij} \frac{(z_i - z_0)}{\sum_k (z_k - z_0)^2} \Delta p_{ij} = -\tau$ where the sums on i and k comprise the aligned objects and the sum on j their active alignment parameters Δp_{ij}.

4.5 Computing optimisations

The MILLEPEDE II program proceeds in a two-step approach. First, the standard CMS software environment [5] is used to produce binary files containing the residuals $m_{ij} - f_{ij}$, their dependence on the parameters $\mathbf{\Delta p}$ and $\mathbf{\Delta q}$ of the linearised track model, the uncertainties σ_{ij}, and labels identifying the fit parameters. Second, these binary files are read by an experiment-independent program that sets up Equation (2), extends it to incorporate the Lagrangian multipliers to implement constraints, and solves it, e.g. by the iterative MINRES algorithm[2] [34]. Since the convergence speed of MINRES depends on the Eigenvalue spectrum of the matrix $\mathbf{C}'$, preconditioning is applied using the inverse of its diagonal. The elements of the symmetric matrix $\mathbf{C}'$ require in general storage in double precision while they are summed up. For the 200 000 alignment parameters used in this study this would require 160 GB of RAM. Although the matrix is rather sparse and only non-zero elements are stored, the reduction is not sufficient. High alignment precision also requires the use of many millions of tracks of different topologies that have to be fit several times within MILLEPEDE II, leading to a significant contribution to the CPU time. To cope with the needs of the CMS tracker alignment described in this article, the MILLEPEDE II program has been further developed, especially to reduce the computer memory needs, to enlarge the number of alignment parameters beyond what was used in [11], and to reduce the processing time. Details are described in the following.

Since the non-zero matrix elements are usually close to each other, further reduction of memory needs is reached by bit-packed addressing of non-zero blocks in a row. In addition, some matrix elements sum contributions of only a few tracks, e.g. cosmic ray tracks from rare directions. For these elements, single precision storage is sufficient.

Processing time is highly reduced in MILLEPEDE II by shared-memory parallelisation using the OpenMP® package [35] for the most computing intensive parts like the product of the huge matrix $\mathbf{C}'$ with a vector for MINRES, the track fits for the calculation of $\mathbf{\Delta q}_j$ and $\mathbf{C}_j^{-1}$, and the construction of $\mathbf{C}'$ from those. Furthermore, bordered band matrices $\mathbf{C}_j$ are automatically detected and root free Cholesky decomposition is applied subsequently (see Section 4.1).

Reading data from local disk and memory access are further potential bottlenecks. The approximations in the track model (see Section 4.1) also aim to alleviate the binary file size. To further reduce the time needed for reading, MILLEPEDE II reads compressed input and caches the information of many tracks to reduce the number of disk accesses.

[2] Note that in contrast to other fast algorithms for solving large matrix equations, MINRES does not require a positive definite matrix and that due to the Lagrangian multipliers $\mathbf{C}'$ is indefinite.

5 Strategy of the internal alignment of the CMS tracker

In general the tracker has been sufficiently stable throughout 2011 to treat alignment parameters as constant in time. The stability of large structures has been checked as decribed in Section 6. An exception from this stability is the pixel detector whose movements have been carefully monitored and are then treated as described below. Validating the statistical alignment precision using the methods of Section 7 shows no need to have time dependent module parameters. Also calibration parameters like those accounting for the Lorentz drift of the charge carriers in the silicon due to the magnetic field influence the reconstructed position of a hit on a module. Nevertheless, for 2011 data there is no need to integrate the determination of calibration parameters into the alignment procedure. The hit position effect of any miscalibration is compensated by the determined alignment corrections. As long as the calibration parameters are stable with time, the exact miscalibration has no influence on the statistical precision. Again, no relevant degradation of this precision with time has been observed.

Given this stability, the 2011 alignment strategy of the CMS tracker consists of two steps, both using the techniques and tools described in Section 4. The first step uses data collected in 2011 until end of June, corresponding to an integrated luminosity of about 1 fb^{-1}. This step is based on the full exploitation of different track topologies, making use of resonance mass and vertex information. The details are described in the rest of this section. The second step treats the four relevant movements of the pixel detector after the end of June, spotted using the methods of Section 6.2. Six alignment parameters for each BPIX layer and FPIX half-disk are redetermined by a standalone alignment procedure, keeping their internal structures and the positions of the strip modules constant.

Tracks from several datasets are fed simultaneously into the alignment procedure. Hit and track reconstruction are described in [21] and the following selection criteria are applied:

- **Isolated muons**: *Global muons* [13] are reconstructed in both the tracker and the muon system. They are selected if their number of hits N_{hit} in the tracker exceeds 9 (at least one thereof in the pixel detector, $N_{hit}(\text{pixel}) \geq 1$), their momenta p are above $8\,\text{GeV}/c$ and their transverse momenta p_T above $5\,\text{GeV}/c$. Their distances $\Delta R = \sqrt{\Delta\varphi^2 + \Delta\eta^2}$ to the axis of reconstructed jets have to be larger than 0.1. About 15 million of these tracks are used for the alignment.
- **Tracks from minimum bias events**: a minimum bias data sample is selected online with a combination of triggers varying with pile-up conditions, based e.g. on pick-up signals indicating the crossing of two filled proton bunches, beam scintillator counters, or moderate requirements on hit and track multiplicity in the pixel detectors. The offline track selection requires $N_{hit} > 7$, $p > 8\,\text{GeV}/c$. Three million of these tracks are used for alignment.
- **Muons from Z^0 decays**: events passing any trigger filter requesting two muons reconstructed online are used for reconstructing Z^0 candidates. Two muons with opposite charge must be identified as *global muons* and fulfil $N_{hit} > 9$ ($N_{hit}(\text{pixel}) \geq 1$). Their transverse momenta must exceed $p_\text{T} > 15\,\text{GeV}/c$ and the invariant mass of the reconstructed dimuon system must lie in the range $85.8 < M_{\mu^+\mu^-} < 95.8\,\text{GeV}/c^2$. 375 000 of these muon pairs are used.
- **Cosmic ray tracks**: cosmic ray events used in the alignment were recorded with the strip tracker operated both in peak and deconvolution mode. Data in peak mode were recorded in a dedicated cosmic data taking period before the restart of the LHC operations in 2011 and during the beam-less times between successive LHC

fills. In addition, cosmic ray data were taken in deconvolution mode both during and between LHC fills, making use of a dedicated trigger selecting cosmic ray tracks passing through the tracker barrel. In total 3.6 million cosmic ray tracks with $p > 4\,\text{GeV}/c$ and $N_{hit} > 7$ are used, almost half of them with the strip tracker operated in peak mode.

Common to all the datasets, basic quality criteria on the hits used in the track fit and on the tracks themselves are applied:

- the signal-over-noise ratio of the strip hits must be higher than 12 (18) when the strip tracker records data in deconvolution (peak) mode,
- for pixel hits, the probability of the hit to match the expected shape of the cluster for the given track parameters [36] must be higher than 0.001 (0.01) in the u (v) direction,
- for all hits, the angle between the track and the module surface must be larger than 10° (20°) for tracks from proton-proton collisions (cosmic rays) to avoid a region where hit position and uncertainty reconstruction are less reliable,
- to ensure a reliable determination of the polar track angle, θ, at least two hits of a track have to lie on pixel or strip stereo modules,
- tracks from proton-proton collisions have to be assigned the "high purity" quality [21] of the CMS track reconstruction code,
- in the final track fit within MILLEPEDE II, tracks are rejected if their χ^2 value is larger than the 99.87% quantile (corresponding to three standard deviations for $N_{dof} = 1$) of the χ^2 distribution for the number of degrees of freedom N_{dof} of the track.

The tracker geometry as determined by the alignment using the 2010 data [29] is the starting point of the 2011 alignment procedure. In general, for each sensor all nine parameters are aligned. Exceptions are v for strip sensors since it is orthogonal to the measurement direction, and the surface parametrisation parameters w_{10}, w_{01}, w_{20}, w_{11}, w_{02} for FPIX modules. The latter is due to their small size and smaller sensitivity compared to the other subdetectors caused by the smaller spread of track angles on the module surface.

The hierarchical alignment approach introduced in Section 4.3 is utilised by introducing parameters for shifts and rotations of half-barrels and end-caps of the strip tracker and of the BPIX layers and FPIX half-disks. For the parameters of the BPIX layers and FPIX half-disks the differential alignment is used as well. The need for nine time periods (including one for the cosmic ray data before the LHC start) has been identified using the validation procedure of Section 6.2. The parameters for the six degrees of freedom of each of the two TOB half-barrels are constrained to have opposite sign, fixing the overall reference system.

Three approaches have been investigated to overcome the twist weak mode as introduced in Section 4.4. The first uses tracks from cosmic rays, recorded in 2010 when the magnetic field was off. This succesfully controls the twist, but no equivalent data was available in 2011. Second, the twist has been measured in the starting geometry using the method of Section 9.2. An equality constraint has been introduced to compensate it. While this method controls the twist, it does not reduce the azimuthal dependence seen in the Sections 9.1 and 9.2. Therefore the final alignment strategy uses the muons from Z^0 decays to include mass information and vertex constraints into the alignment procedure as described in Section 4.4. The value of the virtual mass measurement of $M_{\mu^+\mu^-} = 90.86 \pm 1.86\,\text{GeV}/c^2$ has been deduced from simulated Z^0 decays after final state radiation.

In total, more than 200 000 alignment parameters are determined in the common fit, using 138

constraints. To perform this fit, 246 parallel jobs produce the compressed input files for the MILLEPEDE II program, containing residuals, uncertainties and derivatives for the linearised track model. Their total size is 46.5 GB. The matrix $\mathbf{C}'$ constructed from this by MILLEPEDE II contains 31% non-zero off-diagonal elements. With a compression ratio of 40% this fits well into an affordable 32 GB of memory. The MINRES algorithm has been run four times with subsequently tighter rejection of bad tracks. Since $\mathbf{C}'$ is not significantly changed by this rejection, it does not need to be recalculated after the first iteration. Using eight threads on an Intel® Xeon® L5520 processor with 2.27 GHz, the CPU usage was 44.5 h with a wall clock time of only 9:50 h. This procedure has been repeated four times to treat effects from non-linearity, which is particularly important for eliminating the twist weak mode.

6 Monitoring of the large structures

A substantial fraction of the analyses at CMS uses data reconstructed immediately after the acquisition (*prompt reconstruction*) for obtaining preliminary sets of results. Therefore, it is important to provide to the physics analyses the best possible geometry for use in the prompt reconstruction, correcting immediately any possible time-dependent large misalignment that is present during the data taking. In particular, the position of the large structures in the pixels is relevant for the performance of b-tagging. As described in [37], misalignment at the level of few tens of microns can seriously affect the b-tagging performances.

In order to obtain the best possible performance of the track reconstruction, the tracker geometry is carefully monitored as a function of time, so that corrections can be applied upon movements large enough to significantly affect the reconstruction. The software and reconstruction framework of CMS accommodates time-dependent alignment and calibration conditions by Intervals Of Validity (IOV), which are periods during which a particular set of constants retain the same values [5]. While the alignment at the level of the single modules needs data accumulated over substantial periods of time, the stability of the position of the large structures can be controlled with relatively small amounts of data or via a system of infrared lasers. The short times of data aquisition required by these monitoring methods allow a fast and frequent feedback to the alignment procedure. A system of laser beams is able to monitor the position of a restricted number of modules in the silicon strip tracker. Movements of large structures in the pixel tracker can be detected with high precision with collision tracks by a statistical study of the *primary vertex residuals*, defined as the distance between the tracks and the primary vertex at the point of closest approach of the tracks to the vertex.

6.1 Monitoring of the strip tracker geometry

The CMS Laser Alignment System (LAS) [38] provides a source of alignment information independent from tracks. It is based on 40 near-infrared (1075 nm) laser beams passing through a subset of the silicon sensors that are used for the tracking (see Figure 1). The beams are mounted on mechanical structures independent from those used to support the Tracker. With this limited number of laser beams one can align large scale structures such as TOB, TIB, and both TECs. The mechanical accuracy of LAS components limits the absolute precision of this alignment method to $\sim 50\,\mu$m in comparison to the alignment with tracks, which reaches better than $10\,\mu$m resolution, but the response time of the LAS is at the level of only a few minutes. Within this margin of accuracy, the LAS measurement demonstrates a very good stability of the strip detector geometry over the whole run period. This observation is confirmed by a dedicated set of alignments with tracks, where the dataset was divided in different time periods. No significant movements of the large structures of the Silicon Strip Tracker were found.

6.2 Monitoring of the pixel detector geometry with tracks

The large number of tracks produced in a pp collision allows precise reconstruction of the interaction vertices [12]. The resolution on the reconstructed vertex position is driven by the pixel detector since it is the sub-structure which is closest to the interaction point and has the best hit resolution. The primary vertex residual method studies the distance between the track and the vertex, the latter reconstructed without the track under scrutiny (*unbiased track-vertex residual*). Events used in this analysis are selected online with minimum bias triggers as mentioned in Section 5. The analysis uses only vertices with distances from the nominal interaction point $\rho_{vtx} < 2$ cm and $|z_{vtx}| < 24$ cm in the transverse and longitudinal direction, respectively. The fit of the vertex must have at least 4 degrees of freedom. For each of these vertices, the impact parameters are measured for tracks with:

- more than 6 hits in the tracker, including at least 2 in the pixel detector,
- at least one hit in the first layer of BPIX or first disk of FPIX,
- $p_T > 1\,\mathrm{GeV}/c$,
- $\chi^2/\mathrm{N_{dof}}$ of the track smaller than 5.

The vertex position is recalculated excluding the track under scrutiny from the track collection. A deterministic annealing clustering algorithm [39] is used in order to make the method robust against pile-up, as in the default reconstruction sequence.

The distributions of the unbiased track-vertex residuals in the transverse plane, $\tilde{d}_{xy}$, and in the longitudinal direction, $\tilde{d}_z$, are studied in bins of η and φ of the track. Random misalignments of the modules affect only the resolution on the unbiased track-vertex residual, increasing the width of the distributions, but without biasing their mean. Systematic movements of the modules will bias the distributions in a way that depends on the nature and size of the misalignment and the η and φ of the selected tracks. The dependence of the mean of the $\tilde{d}_{xy}$ and $\tilde{d}_z$ distributions as a function of the azimuthal angle of the track is shown in Figure 6. The focus on the φ-dependence is motivated by the design of the BPIX, which is divided into one half-shell with modules at $\varphi \in [-\pi/2, \pi/2]$ and another with modules at $\varphi \in [\pi/2, \pi] \cup [-\pi, -\pi/2]$. Small movements of the two half-shells are mechanically allowed by the mechanical design of the pixel detector. The observed movements have not been associated to a specific cause, although thermal cycles of the pixel detector increase the chances of this to happen. As example, the impact of a movement of one half-shell with respect to the other in the longitudinal direction is shown by the open circles in Figure 6 for a simulated sample of Minimum Bias events. Such a movement is reflected in a very distinctive feature in the dependence of the mean of the $\tilde{d}_z$ distribution as a function of φ. The size of the movement can be estimated as the average bias in the two halves of BPIX. The time dependence of this quantity in the 2011 data is shown in Figure 7, showing some discontinuities in time. Studies on simulated data show that the b-tagging performance is visibly degraded in the case of uncorrected shifts with amplitude $|\Delta z| > 20\,\mu$m [37]. For this reason, IOVs with different alignments of the pixel layers are defined according to the boundaries of periods with steps of $|\Delta z|$ larger than $10\,\mu$m. The time-dependent alignment parameters of BPIX layers and FPIX half-disks during the first eight IOVs (until end of June) were determined in a single global fit. Within each time interval, the position of the modules with respect to the structure was found to not need any further correction. Because of this, the positions of the pixel layers and half-disks were determined by a separated alignment procedure keeping the other hierarchies of the geometry unchanged. The aligned geometry performs well over the entire data taking period, reducing the observed jumps in the expected way. Residual variations can be attributed to small misalignments with negligible impact on

physics and the resolution of the validation method itself.

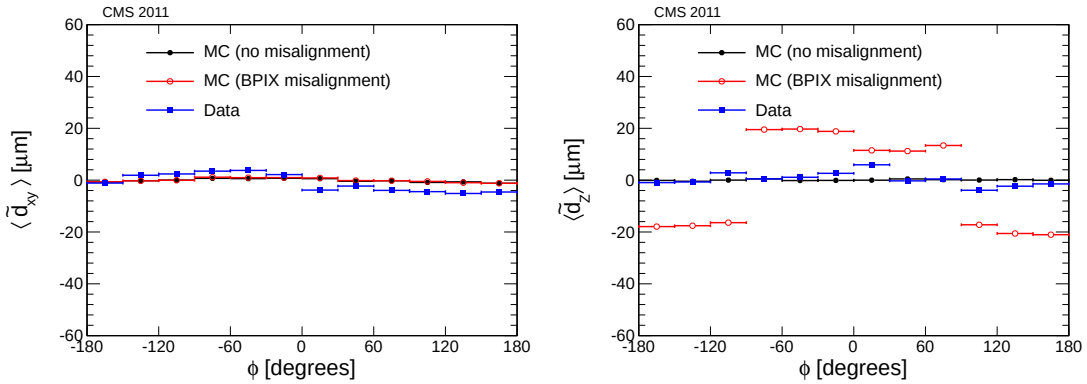

Figure 6: Mean of the distributions of the unbiased transverse (left) and longitudinal (right) track-vertex residuals as a function of the azimuthal angle of the track. Blue squares show the distribution obtained from 10k minimum bias events recorded in 2011. Full circles show the prediction using a simulation with perfect alignment. Open red circles show the same prediction using in the simulation a geometry with the two BPIX half-shells shifted by 20 μm in opposite z-directions.

7 Statistical alignment accuracy

A method for assessing the achieved statistical precision of the aligned positions in the sensitive direction of the modules has been succesfully explored and adopted in the alignment of the Tracker during commissioning with cosmic rays, described in [11]. The results from the validation are based on isolated muon tracks with a transverse momentum of $p_{\mathrm{T}} > 40\,\mathrm{GeV}/c$ and at least ten hits in the tracker. The tracks are refitted using the new alignment constants. Hit residuals are determined with respect to the track prediction, which is obtained without using the hit in question to avoid any correlation between hit and track. From the residual distribution of the unbiased hit residuals in each module, the median is taken and histogrammed for all modules in a detector subsystem. The median is relatively robust against stochastic effects from multiple scattering, and thus the distribution of medians of residuals (DMR) is a measure of the alignment accuracy. Only modules comprising at least 30 entries in their residual distribution are considered.

The addition of proton-proton collision events leads to a huge increase of the number of tracks available for the alignment, especially for the innermost parts of the tracker. Compared to the alignment with cosmic rays alone [11], considerable improvements are indeed observed in the pixel tracker, especially in the endcaps. The corresponding DMR are shown in the lower plots of Figure 8, separately for the u and v coordinates; their RMS is well below 3 μm in both directions, compared to about 13 μm for the endcaps in the cosmic ray-only alignment. These numbers are only slightly larger than the ones obtained in simulation without any misalignment, which are between 0–2 μm, and far below the expected hit resolution. Even in case of no misalignment, the remaining DMR width is non-zero due to statistical fluctuations reflecting the limited size of the track sample. Thus, the DMR width of the no-misalignment case indicates the intrinsic residual uncertainty of the DMR method itself. The remaining uncertainty after alignment determined from real data is close to the sensitivity limit of the DMR method. The kinematic properties of the simulated muon sample are similar but not exactly identical to those of the real data sample, which should be noted for the comparison.

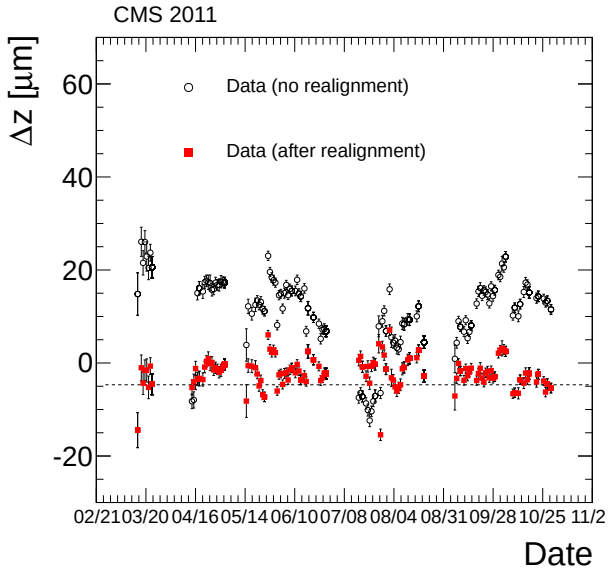

Figure 7: Day-by-day value of the relative longitudinal shift between the two half-shells of the BPIX as measured with the primary vertex residuals. Full marks show the shift observed using the data coming from the prompt reconstruction in 2011. The same events were re-reconstructed after the 2011 alignment campaign, which accounts for the major changes in the positions of the half-shells.

The alignment accuracy of the strip detector is investigated in smaller groups of sensors with a different method using normalised residuals. Each group consists of sensors that are expected to have similar alignment accuracy. The distinction is by layer ("L") or ring ("R") number, by longitudinal hemisphere ("+" and "-" for positive and negative z coordinate, respectively), and according to whether the surface of a barrel module points inwards ("i"), i.e. towards the beamline, or outwards ("o"). The method applied here is based on the widths of the unbiased normalised residual distributions of each sensor group. Since the misalignment dilutes the apparent hit resolution, its degree can be derived from the widening of these normalised residual distributions. The analysis is performed in small intervals of the predicted residual resolution, excluding the hit in question. The alignment uncertainty is added in quadrature to the intrinsic hit resolution of the cluster, and adjusted such that the width of the normalised residual distributions matches the ideal one, which is determined from simulated events. In this way, misalignment in all degrees of freedom of the modules is contributing to the measure. Since the width of the normalised residual distributions is also influenced by the alignment uncertainties of the surrounding detector areas, the procedure is iterated. In each iteration, a damping factor of 0.6 is applied to the correction to mitigate oscillations. Convergence is achieved after 15 iterations.

The resulting alignment accuracy per sensor group, $\sigma_{\mathrm{align,x}}$, is shown in Figure 9 for the TIB, TID and TEC subsystems. In all cases a significant improvement due to the alignment procedure is observed. The alignment accuracy is between 3–8 μm for TIB, between 6–10μm for TID and better than 13 μm for the TEC. The only exception in ring 7 of the TEC is well understood; it is due to a small misplacement of these sensors in the (almost insensitive) radial direction, which has been corrected for further alignment procedures. For large parts of the TOB and the pixel detector, the remaining misalignment cannot be distinguished from zero within the systematic limitations of this method.

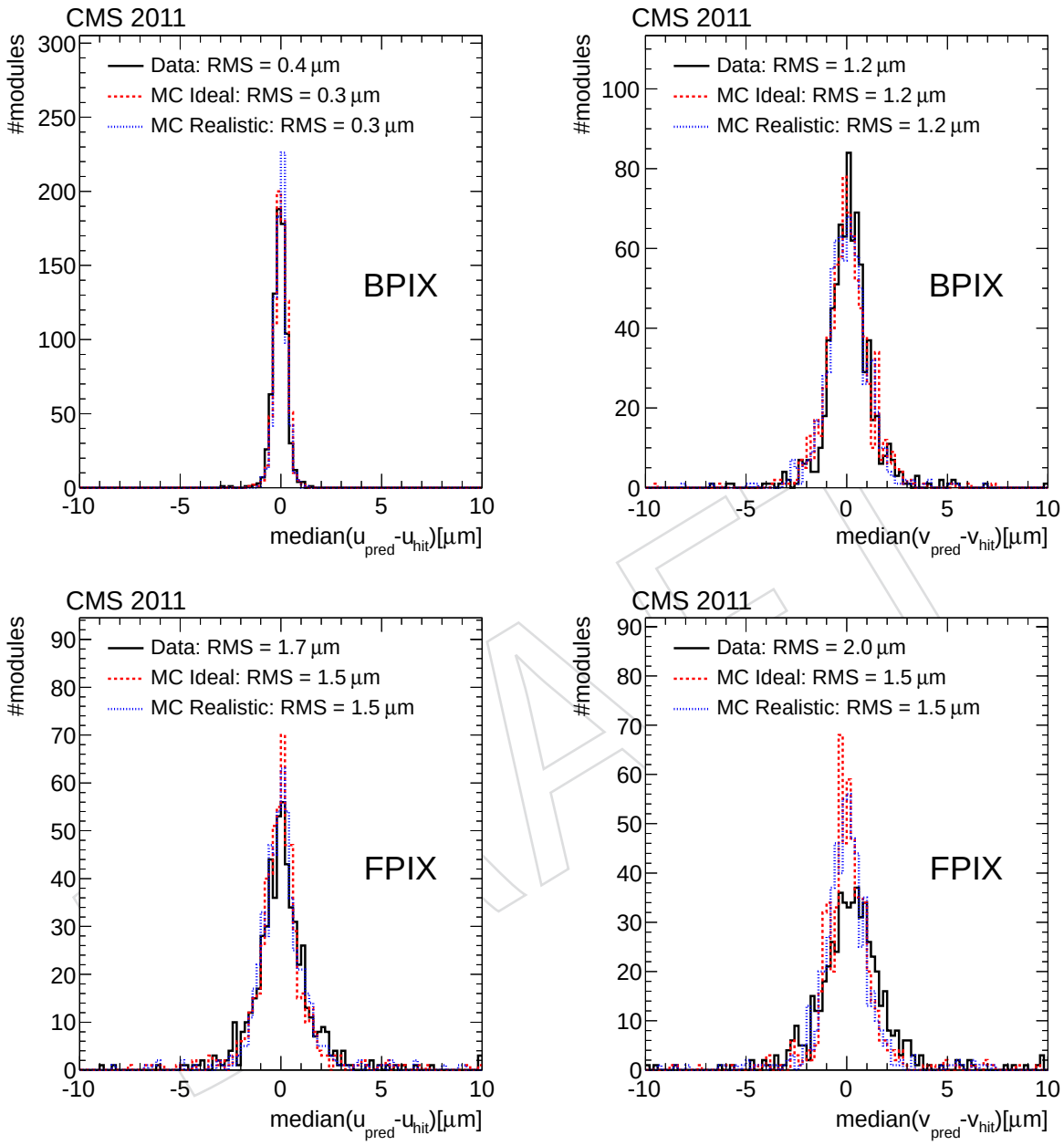

Figure 8: Distributions of the medians of the residuals, for the pixel tracker barrel (top) and endcap modules (bottom) in u (left) and v coordinates (right). Shown in each case are the distributions after alignment with 2011 data (black solid line), in comparison with simulations without any misalignment (red dashed line) and simulation tuned to reproduce the misalignment after the 2011 alignment procedure.

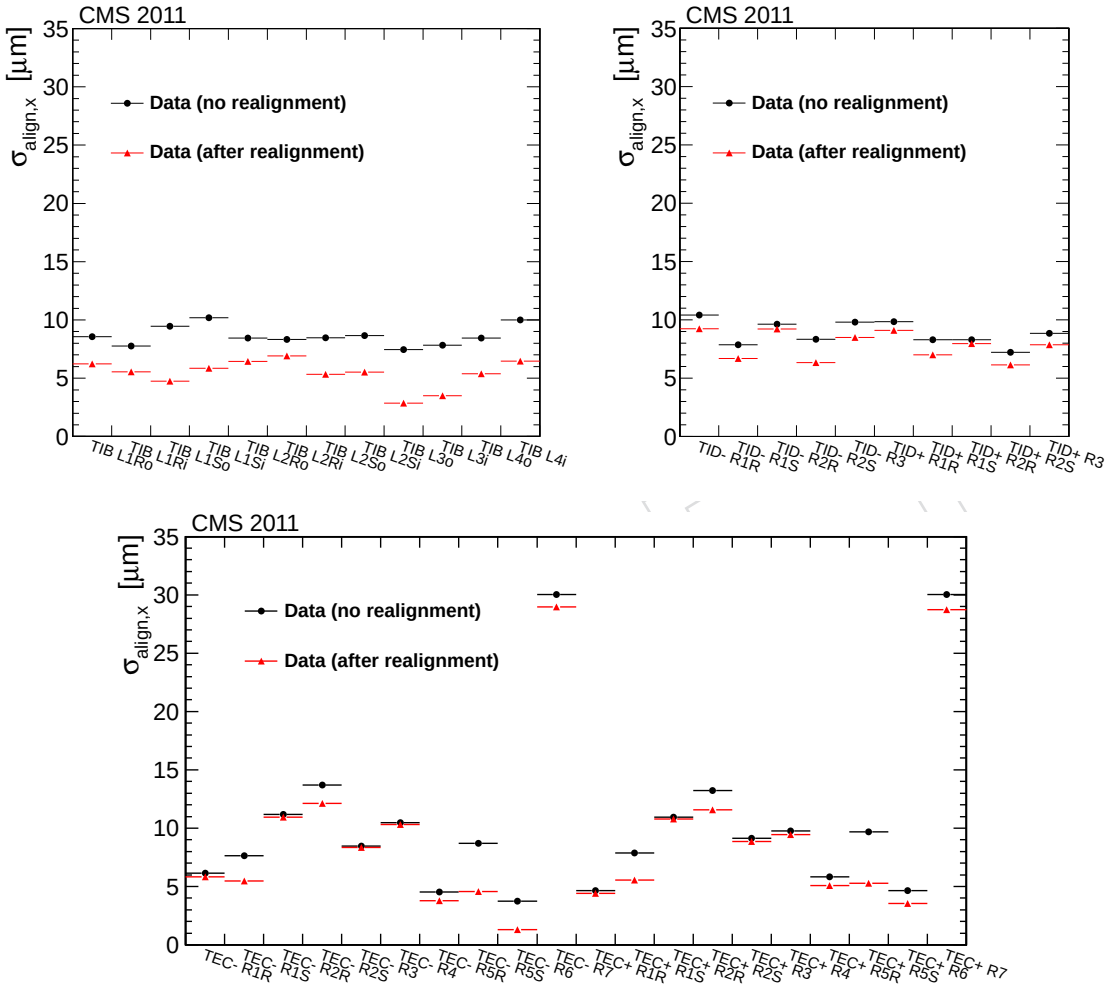

Figure 9: Alignment accuracy in the sub-detectors TIB, TID and TEC, determined sector by sector, using the normalised residuals method. The black symbols show the alignment accuracy before the dedicated alignment with the 2011 data, with the older alignment constants used in the prompt reconstruction, while the red symbols are obtained with the dedicated alignment applied in the reprocessing of the data.

Overall, the statistical accuracy of the alignment is such that its effect is small compared to the intrinsic measurement precision of the sensors. It should be noted, however, that quality estimators based on track residual distibutions have little or no sensitivity to weak modes; these will be addressed in Section 9 of this paper.

8 Sensor and module shape parameters

As discussed in Section 4.2, the tracker modules are not expected to be absolutely flat. If a silicon module is not flat, the local w-coordinate of the point where a track intersects the sensor (see Figure 2) depends on the relative position (u_r, v_r). The module shape can thus be investigated by track-hit residuals in w as a function of the track position on the module [28]. These residuals can be calculated from the one in the u-direction and the track angle ψ (Figure 2), $\Delta w = \Delta u / \tan\psi$. The mean values of these residuals for cosmic ray tracks are shown in Figure 10 as a function of the relative local track coordinates u_r and v_r, averaged over many modules of the strip subdetectors. Since tracks with a large angle ψ relative to the surface normal are most sensitive to any deviation from flatness, each residual in the average is weighted by $\tan^2\psi$. The CMS track reconstruction algorithm treats the hits under the assumption of a flat module surface. To compensate for the deviation from flatness, the reconstructed hit positions in u are corrected by $-w\tan\psi$ where the local w is calculated from the point (u_r, v_r) where the track crosses the module and from the module dependent coefficients determined for the respective parametrisation.

Several module shape parametrisations are investigated in the alignment procedure as shown in Figures 10 and 11. The magenta open circles are deduced using alignment constants achieved in a procedure similar to the one described in Section 5, but without taking any module shape parameters into account. Clear deviations from zero are observed in almost all cases, indicating that the modules are not flat. The red filled triangles are obtained with the same alignment procedure except that the two sensors of the modules in the TOB and in the TEC rings 5-7 are aligned independently. The blue open triangles do not treat these sensors separately, but uses the polynomials described in Section 4.2 to parametrise the module surfaces as a whole. Finally, the black points represent the final alignment, i.e. treating each sensor independently and as possibly curved. Table 1 summarises the different levels of module shape correction.

Table 1: Nomenclature for different levels of shape correction.

Treatment of modules with		Curvature	Kinks/shifts
one sensor	two sensors		between sensors
Flat	Flat modules	–	–
	Flat sensors	–	X
Curved	Curved modules	module level	–
	Curved sensors	sensor level	X

For the distributions along u_r for Flat Modules, a parabolic shape of the sensors of all subdetectors is clearly observed. These structures are correctly compensated when curvatures are taken into account as for the Curved Sensors. At the largest values of $|u_r|$ in the TEC there are few tracks since the modules are wedge-like shaped and their widthes l_u are defined by their longer edges. The distributions along the strip direction (v_r) show more varied features. In the TIB, a structure remains that could be corrected by a fourth order polynomial, but the amplitude is only a few μm and thus negligible for tracking purposes. For the TOB, the V-shaped curve

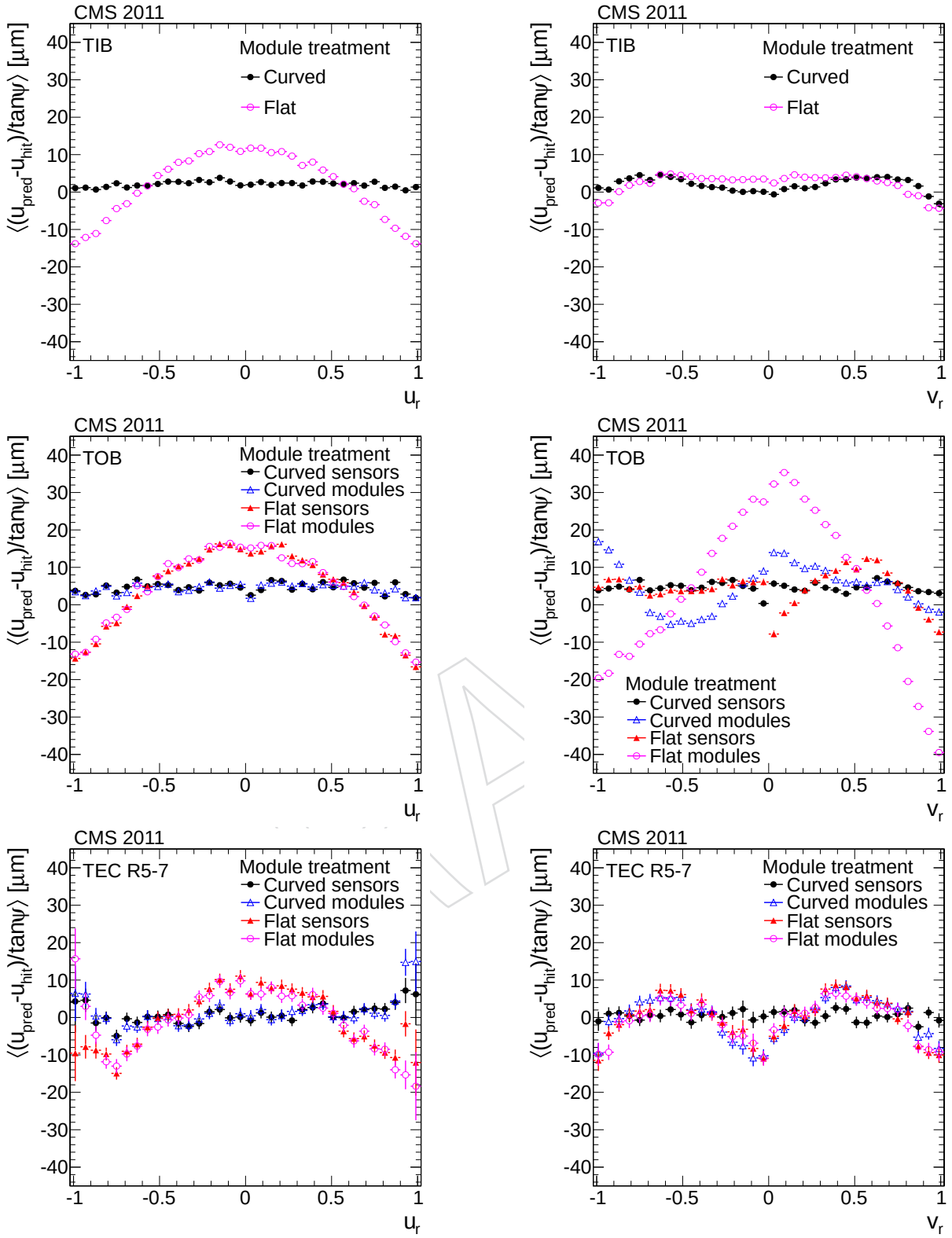

Figure 10: Distributions of the weighted means of the $\Delta w = \Delta u / \tan\psi$ track-hit residuals as a function of the relative position of cosmic ray tracks on the modules along the local u- (left) and v-axis (right) for different approaches to parametrise the module shape. The first two rows show the average for all the TIB and TOB modules, respectively, and the last row shows the double sensor modules of the rings 5-7 of the TEC. Each residual is weighted by $\tan^2\psi$ of the track.

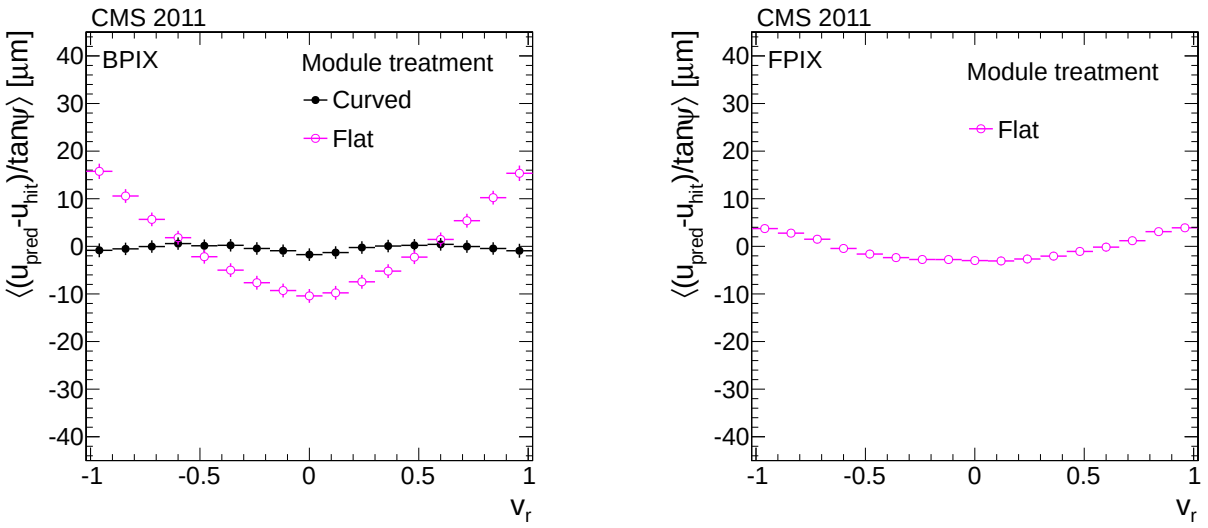

Figure 11: Distributions of the weighted means of the $\Delta w = \Delta u / \tan\psi$ track-hit residuals as a function of the relative position of tracks from proton-proton collisions on the modules along the local v-axis for different approaches to parametrise the module shapes. The left shows the BPIX and the right the FPIX. Each residual is weighted by $\tan^2\psi$ of the track.

of the Flat Modules parametrisation indicates a kink between the two sensors of the modules. After correcting for the relative misalignment of the sensors using the Flat Sensors parametrisation, a parabolic shape can be seen for the sensors at positive v_r. The parametrisation as Curved Modules finds an effective correction that reduces the effect of the module kink, but only the use of the Curved Sensors correction level results in a flat dependence. For the double sensor modules in the TEC rings 5-7, no relevant kink between the sensors is visible. But clearly both sensors are curved, as taken into account using the Curved Sensors parametrisation.

In the pixel detectors, no systematic structure is observed along the u-direction. The mean w-residual distributions along the v-direction, determined with tracks from proton-proton collisions, is shown in Figure 11. A curvature of the BPIX modules, with opposite sign compared to the strip subdetectors, can clearly be seen. Also the FPIX modules show curvatures, but with smaller amplitude. No corrections are necessary for this subtle effect.

The Curved Sensor parametrisation leads to a sizable improvement of the quality of tracks that cross modules with large angles relative to the module normal. Especially cosmic ray tracks crossing the barrel of the tracker from the top to the bottom with large distances of closest approach to the beam line d_0 predominantly have these large track angles. Figure 12 shows the average fit probability $\langle \mathrm{Prob}(\chi^2, \mathrm{N_{dof}}) \rangle$ as a function of $|d_0|$ for cosmic ray tracks. Tracks with small $|d_0|$ cross the modules with modest angles relative to the normal. With larger $|d_0|$, also the average angle of incidence of the track with respect to the module increases, resulting in a significant degradation of the average fit quality for the Flat Modules parametrisation. For Curved Sensors the distribution is approximately flat for $|d_0| < 50\,\mathrm{cm}$, resulting in an improved consistency of the important cosmic ray track sample with tracks from proton-proton collisions. The remaining features of the dependence are correlated with the radii of the barrel layers. If tracks cross a layer tangentially, the treatment of multiple scattering effects using thin scatterers only is an oversimplified approximation.

The average size of the determined sensor curvature amplitudes along the u- (w_{20}) and v-direction (w_{02}) are shown in Figure 13 for the different layers and rings, further differentiating

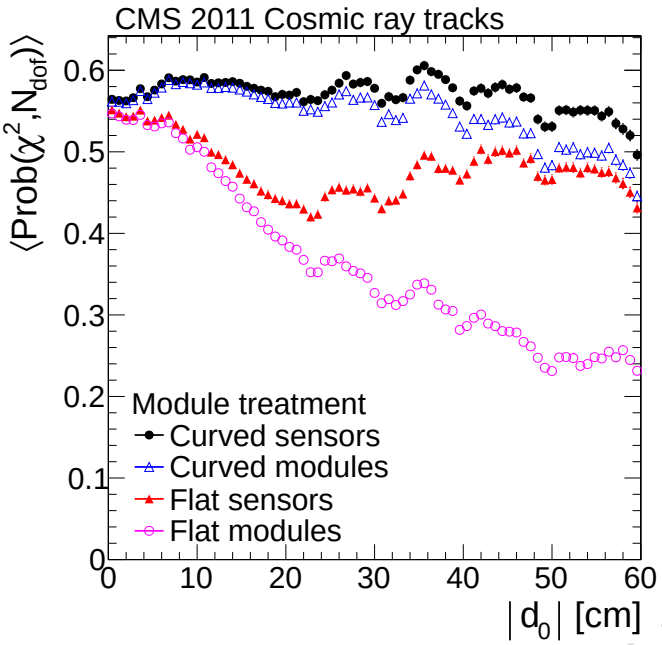

Figure 12: Mean probability $\langle \mathrm{Prob}(\chi^2, \mathrm{N_{dof}}) \rangle$ of cosmic ray track fits as a function of their distance of closest approach to the nominal beam line for the different approaches to parametrise the module shapes.

for stereo and $r\varphi$ modules, i.e. grouping modules with similar sensors and mounting. While the average amplitude $\langle w_{20} \rangle$ for BPIX sensors is almost zero, it is usually around $-30\,\mu$m in the strip subdetectors. This matches well the sagittae of the average module shapes along u seen for the Flat Module distributions on the left of Figure 10. Stronger curvatures up to $\langle w_{20} \rangle < -80\,\mu$m are observed for specific sensor types and mounting positions, e.g. the $r\varphi$ modules in TEC ring 2. The average amplitude $\langle w_{02} \rangle$ shows variations from $+30\,\mu$m for BPIX modules (matching with the left of Figure 11) to almost $-60\,\mu$m for some sensor types in the TEC. While the average sensor curvatures are clearly below the construction specifications of $100\,\mu$m, the tails of distributions extend to $|w_{ij}| > 200\,\mu$m and even beyond.

Aligning both sensors of the modules in the TOB and the TEC rings 5-7 independently reveals that the sensors were slightly misaligned with respect to each other during module assembly. As an example, Figure 14 reveals their average differences of the rotation angles around the local u-axis, $\Delta\alpha = \alpha_1 - \alpha_2$ where the first sensor is the one closer to the readout electronics at $v < 0$. The TOB modules show an average kink of $\langle \Delta\alpha \rangle \approx 1.6$ mrad, matching well the kink seen in the TOB graph *vs.* v of Figure 10. The value significantly differs for the different modules in the TEC. This has averaged out the kink effect in the TEC distribution *vs.* v. The angular misalignment of the two sensors exhibits a significant spread as shown for $\Delta\alpha$ and, for the rotation around v, $\Delta\beta$ of the TOB modules in Figure 15. Values of $\Delta\alpha = 6$ mrad are reached, corresponding to $\Delta w \approx 150\,\mu$m at the edges of the 10 cm long sensors.

In summary, the module shapes can be described using polynomials up to the second order for each sensor, and the their coefficients are successfully determined module-by-module within the alignment procedure. Applying corrections to the hit positions that depend on the determined module parameters and on the track parameters on the module surface, significantly improves the overall track description, especially for the important cosmic ray tracks. The goodness of fit, $\langle \mathrm{Prob}(\chi^2, \mathrm{N_{dof}}) \rangle$, becomes constant up to impact parameters of $|d_0| = 50$ cm, improving the overall consistency with the tracks from proton-proton collisions. The parame-

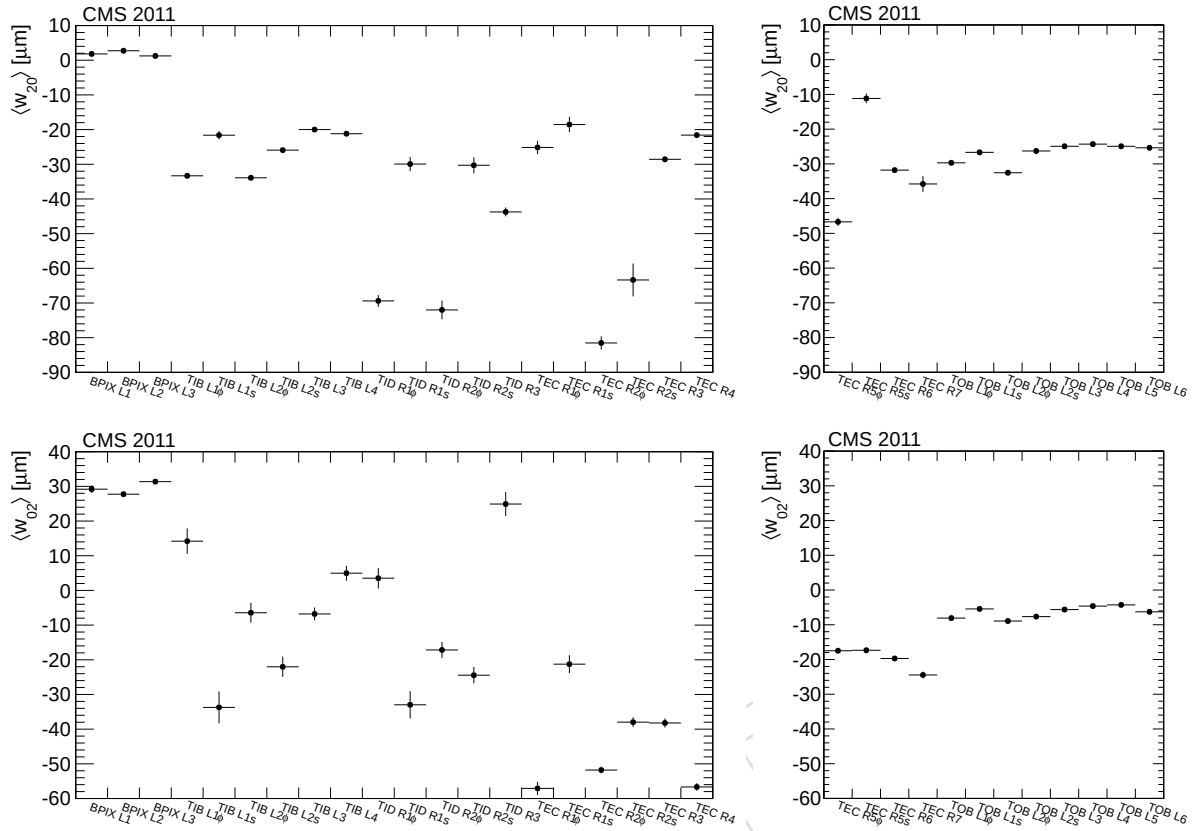

Figure 13: Sensor curvatures along the local u (upper row) and v (lower row) coordinate for single (left column) and double (right columns) sensor modules, averaged over layers (L) and rings (R), respectively. Stereo (s) and $r\varphi$ (ϕ) modules within a layer or ring are separated.

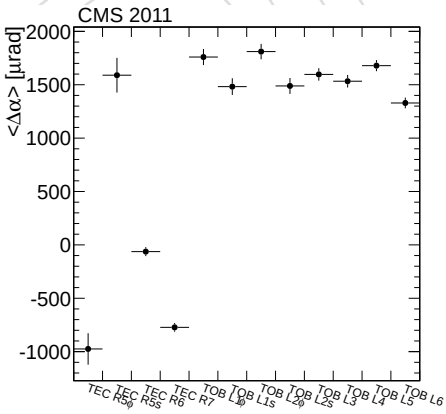

Figure 14: Kink angle $\Delta\alpha$ for double sensor modules, averaged over layers (L) and rings (R), respectively. Stereo (s) and $r\varphi$ (ϕ) modules within the same layer or ring are separated.

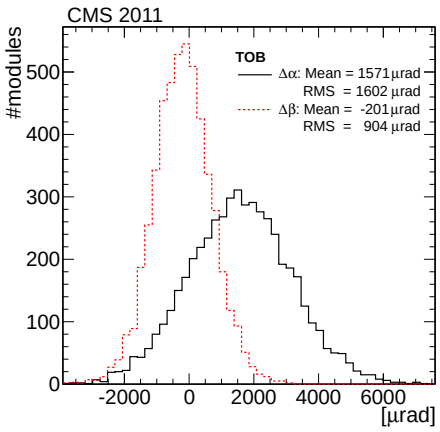

Figure 15: Distributions of the kink angles $\Delta\alpha$ and $\Delta\beta$ of TOB modules.

ters determined in-situ show that the majority of the modules fulfil the construction criterion of sensor bows below 100 μm. The sensor parametrisation used here is valid as long as the effect of the curvatures can be approximated by a change of the local w coordinate only, neglecting changes in u and v. Within these boundaries, the requirement could have been—in retrospect—relaxed since the alignment successfully takes care of this effect.

9 Control of systematic misalignment

The monitoring of standard physics candles and the comparison with other subdetectors of CMS provides a direct check of the robustness of the alignment procedure, and potentially indicates the presence of systematic misalignments. This information can be included in the alignment algorithm in order to better constrain the systematic misalignments, as described in Section 4.4. The sensitivity to weak modes of the alignment procedure followed in this analysis is discussed in Section 9.3 following the approach presented in [11, 28].

9.1 Monitoring of the tracker geometry with $Z^0 \to \mu\mu$ events

As described in Sections 4.4 and 5, muonic decays of Z^0 bosons provide a standard candle that can be used for validating the aligned geometry. The selection of well-reconstructed $Z^0 \to \mu^+\mu^-$ candidates requires two muons reconstructed using both the tracker and the muon system (*global muons*) as described in [13]), where at least one of them passes the tight quality selections as defined in [13]. The muons must pass the following kinematic cuts:

- $p_T > 20\,\text{GeV}/c$,
- $|\eta| < 2.4$,
- $80 < M_{\mu\mu} < 120\,\text{GeV}/c^2$, where $M_{\mu\mu}$ is invariant mass of the dimuon system.

The distribution of the mass of the Z^0 candidates is then fitted with a Voigtian function to model the signal of genuine Z^0, and an exponential function to model the background. The width of the Breit-Wigner component of the Voigtian function is fixed to the decay width of the Z^0 boson. The mass of the Z^0 candidates is estimated with the mean of the fitted Voigtian.[3] The mass of the Z^0 candidates is measured as a function of the η and φ of the muon with positive charge. A twist-like weak mode would bias the curvature measurement of each muon depending on its polar angle, manifesting itself as a strong dependence of the Z^0 mass on the muon pseudorapidity (with opposite signs for the two muon charges).

The result of this study is presented in Figure 16 for both the 2011 data and the simulation, and the corresponding dependence of the Z^0 mass on the difference in pseudorapidity of the two muons, $\Delta\eta = \eta^+ - \eta^-$, is shown in Figure 17. Using the nominal geometry, the estimation of the Z mass in the simulation is at the expected value of $90.8\,\text{GeV}/c^2$. Without using the Z^0 mass information (down-facing triangles), a pronounced η and $\Delta\eta$ dependence of the reconstructed invariant mass is observed, which spans over a range of more than $5\,\text{GeV}/c^2$ and is attributed to a twist weak mode as seen in Section 9.2. The inclusion of the Z^0 mass information (up-facing triangles) removes this bias and leads to an almost flat dependence on η and $\Delta\eta$. The agreement between the data and the simulation is good. A small offset of about $100\,\text{MeV}/c^2$ in the simulation with respect to the data is visible. The size of any remaining bias, also as a function of azimuth angle, is of the order of a few per mille, and thus small compared to the p_T resolution targeted for muons in the typical momentum range of the Z^0 decays, which

[3] With this choice, the reconstructed Z^0 mass is slightly below the nominal mass of $91.2\,\text{GeV}/c^2$, at about $90.8\,\text{GeV}/c^2$ [13].

is at best 1% [13]. Offline corrections to the muon four-momentum can be applied after the reconstruction level, further improving the momentum scale and resolution of the muons [13].

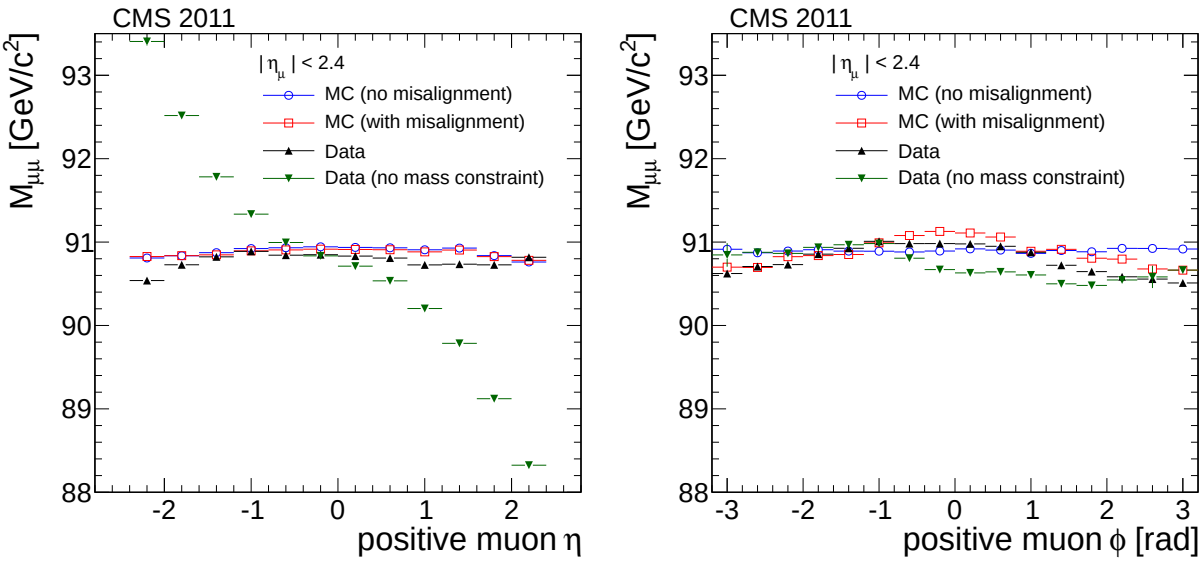

Figure 16: Invariant mass of $Z^0 \to \mu^+\mu^-$ candidates as a function of η (left) and φ (right) of the positively-charged muon. Distributions from aligned data are shown as black up-facing triangles . Distributions from a simulation with perfect alignment and realistic misalignment are presented as blue hollow circles and red hollow markers, respectively. The same distribution using the data but with a geometry produced without the mass constraint is presented with green markers.

9.2 Monitoring of the tracker geometry with the CMS calorimeter

The measurements of the CMS electromagnetic and hadronic calorimeters can be exploited to study systematic effects in the momentum measurement. This check is valuable since it is an alternative to the $Z^0 \to \mu^+\mu^-$ decays which are already used in the alignment procedure. Weak modes altering the true azimuthal angle of the modules would modify the track curvature in an opposite way for positively and negatively charged tracks. In the case of a twist-like deformation, the bias on the p_T of tracks depends on the bias on the φ-position of the hits, $\Delta\varphi$ (corresponding to the rotational misalignment of the layers) :

$$p_T^{\pm} = \frac{0.57\,\text{GeV} \cdot r[\text{m}]}{\sin(\varphi \mp \Delta\varphi)}, \tag{9}$$

where the $\pm$ indicates the electric charge of the particle, $r[\text{m}]$ is the radius (measured in metres) at which the particle leaves the tracker volume. A longitudinal magnetic field strength of 3.8 T is assumed. The strength of the twist is expressed by the relative angle $\Delta\varphi$, and related to the asymmetry in the p_T measurement of oppositely charged tracks with the same true p_T and same θ. An external measurement of the energy of the charged particle, E, is provided by the ECAL and the HCAL [40]. Given the average ratio between the energy and momentum of a charged track at fixed p_T, $\langle E/p \rangle$, $\Delta\varphi$ is measured as a function of the asymmetry between positively and negatively charged tracks, $(\langle E/p^- \rangle - \langle E/p^+ \rangle)$:

$$\Delta\varphi = \frac{1}{2}\left[\arcsin\left(\frac{0.57 \cdot r[\text{m}]}{\langle E \cdot \sin\theta \rangle\,[\text{GeV}]}\left\langle\frac{E}{p^-}\right\rangle\right) - \arcsin\left(\frac{0.57 \cdot r[\text{m}]}{\langle E \cdot \sin\theta \rangle\,[\text{GeV}]}\left\langle\frac{E}{p^+}\right\rangle\right)\right], \tag{10}$$

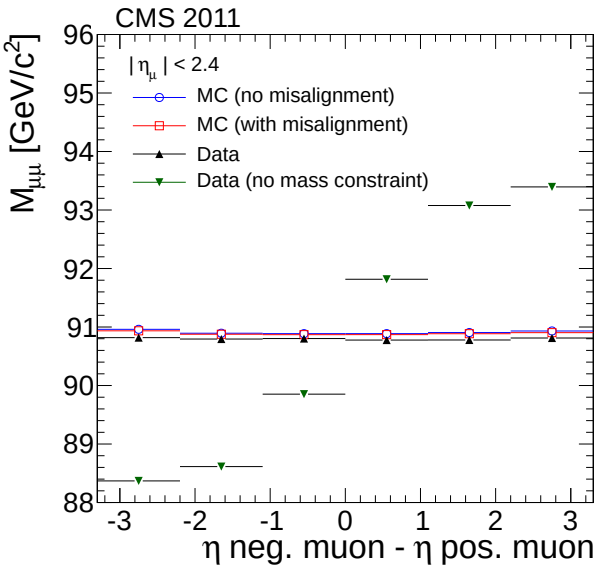

Figure 17: Invariant mass of $Z^0 \to \mu\mu$ candidates as a function of the η separation of the two muons. Distributions from aligned data are shown as black up-facing triangles . Distributions from a simulation with perfect alignment and realistic misalignment are presented as blue hollow circles and red hollow markers, respectively. The same distribution using the data but with a geometry produced without the mass constraint is presented with green markers.

which for large p_T ($p_T \gtrsim 10\,\text{GeV}/c$) and small misalignments ($\Delta\varphi \ll 1$) approximates to

$$\Delta\varphi = \frac{(0.57 \cdot r)}{2} \frac{\left\langle \frac{E}{p^-} \right\rangle - \left\langle \frac{E}{p^+} \right\rangle}{\langle E \cdot \sin\theta \rangle} . \tag{11}$$

The track sample used for the validation is selected from an input dataset of events triggered by requiring a track with a total momentum $p > 38\,\text{GeV}/c$ and matched to an HCAL cluster. A charged track isolation requirement is applied at the trigger level ensuring that no track with a transverse momentum of $p_T > 2\,\text{GeV}/c$ is allowed to be in a circle with a radius of 40 cm around the impact point on the ECAL surface of the considered track. The distributions of $\langle E/p^- \rangle$ and $\langle E/p^+ \rangle$ for particles with similar energy E are fitted with a Gaussian function. The means of the fits are used in Equation (11) in order to measure the $\Delta\varphi$ for that specific bin. The results for different bins of the calorimeter energy are finally averaged. This method uses the calorimetric information only for identifying tracks with the same energy, improving its robustness against miscalibrations of the absolute energy scale of the calorimeters. The dependence of $\Delta\varphi$ on the z of the impact point at the radial position $r = 1\ m$ and on the φ of the track is shown in Figure 18 for different geometries. A twist deformation would show up as a linear trend in the z-dependence. From the z-dependence, no significant systematic distortion in the aligned geometry is visible within the current uncertainties of the validation method. A clear improvement with respect to a geometry not exploiting the mass information is visible. A linear fit to the distributions is performed in order to quantify the bias. In the absence of the mass information in the alignment procedure, the linear fit exhibits a slope significantly different from zero, $351 \pm 12\,\mu\text{rad}/m$. In the case of the baseline alignment on data, the slope is $2 \pm 12\,\mu\text{rad}/m$. Slopes compatible with zero are observed also in the case of the simulation, both without misalignment and with a misalignment similar to the one of the data. A layer rotation,

i.e. a systematic rotation of the layers with an amplitude proportional to the radius ($\Delta\varphi = \rho \cdot (r - r_0)$), would appear as a constant offset. The $\varphi-$dependence displays the same trend as already seen in the validation with $Z^0 \to \mu^+\mu^-$ of Figure 16. The fit to the sinusoidal trend observed in the data distribution gives a parametrization of $(36 \pm 5) \cdot \sin(\varphi + (2.8 \pm 0.2))$ μrad.

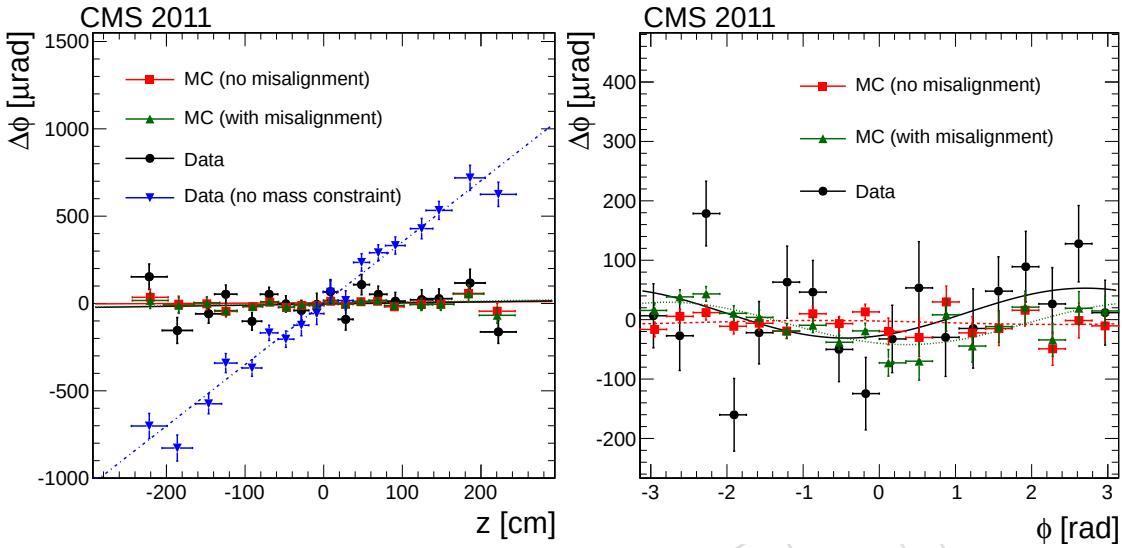

Figure 18: Rotational misalignment, $\Delta\varphi$, as a function of the z-position at $r = 1$ m (left) and φ (right) of the track. Distributions from 2011 data using an aligned geometry are shown as black dots. The distributions from the simulation with perfect alignment and realistic misalignment are presented as red squares and green triangles, respectively. The blue downward-facing triangles in the left figure show the distribution using an alignment obtained without using the information of the Z^0 mass.

9.3 Sensitivity to systematic misalignment

Beyond the validation of the aligned geometry, the sensitivity of the alignment procedure has been studied. Following the approach in [11, 28], a set of basic deformations were applied on top of the aligned tracker geometry. The full alignment procedure was then repeated starting from the misaligned scenario, obtaining a set of "realigned" geometries. Nine systematic misalignment scenarios were studied, giving a matrix of deformations expressed with Δr, Δz and $\Delta\varphi$ as a function of the same three variables. These misalignments were applied only to the directions to which the silicon modules are effectively sensitive. Movements along non-measurement directions (e.g., the longitudinal direction for strip barrel modules) are irrelevant, since the alignment procedure does not associate any parameters with them.

The ability of the alignment procedure to compensate for the misalignments indicates its robustness against systematic distortions of this or similar type. A close match between the realigned and initial geometry means that the procedure is fully sensitive to this specific deformation and able to keep it under control. On the other hand, little or no changes compared to the misaligned scenario indicate poor sensitivity.

Figure 19 displays the difference between the positions of the modules in the initial aligned and the deliberately misaligned geometry for some benchmark misalignment scenarios. The upper, middle and bottom row present the cases of twist, skew and sagitta deformations as introduced in Section 4.4. The results show that the alignment procedure has very good control over twist-like deformations. Such control comes largely from the constraining power of the

muonic Z^0 decays. Skew and sagitta are interesting because they are the systematic distortions most difficult to control. The skew misalignment is fully recovered in the pixel barrel, but not in the other subdetectors. The alignment procedure is only partially resilient to the sagitta distortion, with the best recovery observed at small radii. The other six misalignment scenarios considered proved to be well controlled. These results represent a significant improvement with respect to [11] thanks to the inclusion of tracks from proton-proton collisions with several different topologies and the usage of vertex constraint and mass information with muons coming from Z^0 bosons.

10 Summary

The alignment procedure for the CMS tracker and its results for the first high-luminosity data-taking year are presented. Among its most prominent features are the successful handling of the large degree of complexity of a highly granular silicon detector, the simultaneous determination of shape parameters at the sensor level, the consequent use of the Z^0 resonance signature to control systematic effects, and the parallelised implementation resulting in a fast execution of the workflow.

The alignment is based on global minimisation of track-to-hit residuals. The internal alignment is performed with the MILLEPEDE II algorithm, which is enhanced compared to its predecessor to handle about 200 000 alignment parameters concurrently. A dedicated track parameterisation is included, based on the General Broken Lines method, which allows rigorous and execution time efficient treatment of multiple scattering in the global fit. The execution time of the fit is considerably shortened by parallelisation on a multi-core architecture.

The time dependence of the tracker alignment is monitored with laser beams and tracks. The tracker geometry is found to be very stable with time. The most relevant movements are observed between the half-shells of the pixel detector, whose longitudinal separation varies by up to 40 μm. The alignment procedure corrects for these movements such that the residual variation after alignment is kept below 10 μm.

The overall tilt angles of the tracker with respect to the magnetic field are determined to be at the sub-mrad level. The statistical accuracy of the alignment is found to be generally – often significantly – better than 10 μm, with the exception of some rings in the tracker endcap disks. Sensor and module shape parameters are determined at the module level simultaneously with other alignment parameters. Curvatures of individual sensors and kink angles of adjacent sensors in modules are observed and measured; sensor curvature amplitudes vary according to subsystem, and their averages per layer and ring range up to about 80 μm in the endcap systems. Kink angles of up to several mrad are observed.

Besides cosmic ray tracks, reconstructed $Z^0 \to \mu^+\mu^-$ decays play an essential role in constraining systematic deformations of the aligned geometry with small leverage to the track χ^2, also known as weak modes. The remaining variation of the visible Z^0 mass is less than 0.5%, and thus small compared to other resolution effects in the corresponding momentum range. The achieved suppression of weak modes is confirmed by studies involving the cluster energy measured in the hadronic calorimeter.

The stability of the alignment with respect to weak modes is further investigated by the study of recovery after deliberate addition of distortions and subsequent re-alignment. The procedure is found to have very good control over twist modes, while strong sagitta and skew misalignments are at least partially recovered.

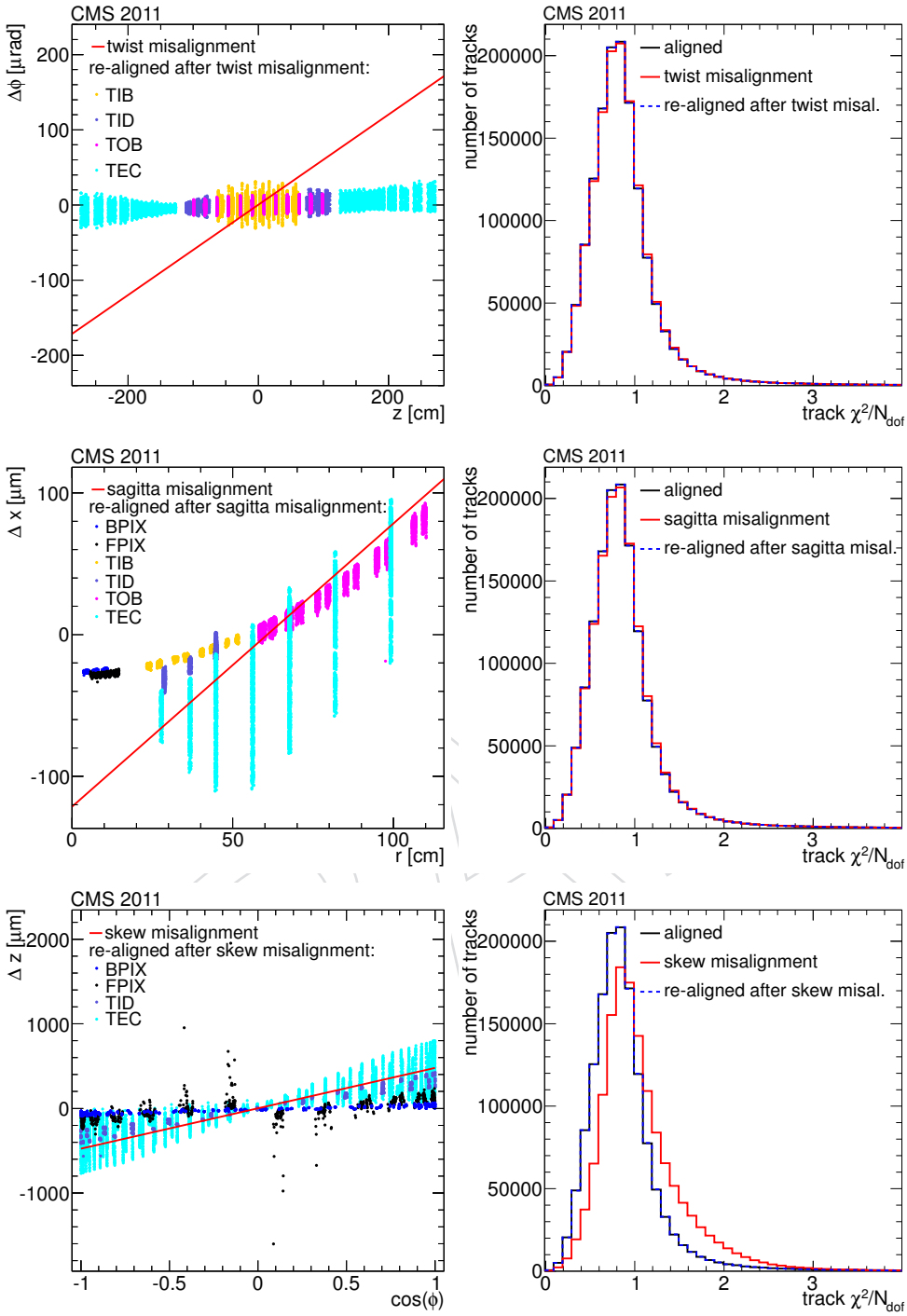

Figure 19: Impact of intentional application of a twist (top row), sagitta (middle row) and skew systematic misalignment (bottom row). In the left columns, the red line shows the size of the applied misalignment, and the coloured dots show the difference of selected geometry parameters, module by module after realignment, to the initial values prior to misalignment. The plots in the right column show the distributions of goodness-of-fit for loosely-selected isolated muons from an independent data sample, with transverse momentum $p_{\mathrm{T}} > 5\,\mathrm{GeV}/c$.

In summary, this article describes the comprehensive alignment procedure for the largest and most complex silicon detectors ever built. The achieved alignment accuracy enables the tracking to take full benefit of the high intrinsic resolution of the silicon modules. The quality of the alignment is thus a pivotal corner stone for the excellent physics performance of the CMS detector.

Acknowledgments

We congratulate our colleagues in the CERN accelerator departments for the excellent performance of the LHC and thank the technical and administrative staffs at CERN and at other CMS institutes for their contributions to the success of the CMS effort. In addition, we gratefully acknowledge the computing centres and personnel of the Worldwide LHC Computing Grid for delivering so effectively the computing infrastructure essential to our analyses. Finally, we acknowledge the enduring support for the construction and operation of the LHC and the CMS detector provided by the following funding agencies: the Austrian Federal Ministry of Science and Research; the Belgian Fonds de la Recherche Scientifique, and Fonds voor Wetenschappelijk Onderzoek; the Brazilian Funding Agencies (CNPq, CAPES, FAPERJ, and FAPESP); the Bulgarian Ministry of Education, Youth and Science; CERN; the Chinese Academy of Sciences, Ministry of Science and Technology, and National Natural Science Foundation of China; the Colombian Funding Agency (COLCIENCIAS); the Croatian Ministry of Science, Education and Sport; the Research Promotion Foundation, Cyprus; the Ministry of Education and Research, Recurrent financing contract SF0690030s09 and European Regional Development Fund, Estonia; the Academy of Finland, Finnish Ministry of Education and Culture, and Helsinki Institute of Physics; the Institut National de Physique Nucléaire et de Physique des Particules / CNRS, and Commissariat à l'Énergie Atomique et aux Énergies Alternatives / CEA, France; the Bundesministerium für Bildung und Forschung, Deutsche Forschungsgemeinschaft, and Helmholtz-Gemeinschaft Deutscher Forschungszentren, Germany; the General Secretariat for Research and Technology, Greece; the National Scientific Research Foundation, and National Office for Research and Technology, Hungary; the Department of Atomic Energy and the Department of Science and Technology, India; the Institute for Studies in Theoretical Physics and Mathematics, Iran; the Science Foundation, Ireland; the Istituto Nazionale di Fisica Nucleare, Italy; the Korean Ministry of Education, Science and Technology and the World Class University program of NRF, Korea; the Lithuanian Academy of Sciences; the Mexican Funding Agencies (CINVESTAV, CONACYT, SEP, and UASLP-FAI); the Ministry of Science and Innovation, New Zealand; the Pakistan Atomic Energy Commission; the Ministry of Science and Higher Education and the National Science Centre, Poland; the Fundação para a Ciência e a Tecnologia, Portugal; JINR (Armenia, Belarus, Georgia, Ukraine, Uzbekistan); the Ministry of Education and Science of the Russian Federation, the Federal Agency of Atomic Energy of the Russian Federation, Russian Academy of Sciences, and the Russian Foundation for Basic Research; the Ministry of Science and Technological Development of Serbia; the Secretaría de Estado de Investigación, Desarrollo e Innovación and Programa Consolider-Ingenio 2010, Spain; the Swiss Funding Agencies (ETH Board, ETH Zurich, PSI, SNF, UniZH, Canton Zurich, and SER); the National Science Council, Taipei; the Thailand Center of Excellence in Physics, the Institute for the Promotion of Teaching Science and Technology and National Electronics and Computer Technology Center; the Scientific and Technical Research Council of Turkey, and Turkish Atomic Energy Authority; the Science and Technology Facilities Council, UK; the US Department of Energy, and the US National Science Foundation.

Individuals have received support from the Marie-Curie programme and the European Research Council (European Union); the Leventis Foundation; the A. P. Sloan Foundation; the

Alexander von Humboldt Foundation; the Belgian Federal Science Policy Office; the Fonds pour la Formation à la Recherche dans l'Industrie et dans l'Agriculture (FRIA-Belgium); the Agentschap voor Innovatie door Wetenschap en Technologie (IWT-Belgium); the Ministry of Education, Youth and Sports (MEYS) of Czech Republic; the Council of Science and Industrial Research, India; the Compagnia di San Paolo (Torino); and the HOMING PLUS programme of Foundation for Polish Science, cofinanced from European Union, Regional Development Fund.

References

[1] CMS Collaboration, "The CMS experiment at the CERN LHC", *JINST* **3** (2008) S08004, doi:10.1088/1748-0221/3/08/S08004.

[2] L. Evans and P. B. (eds.), "LHC Machine", *JINST* **3** (2008) S08001, doi:10.1088/1748-0221/3/08/S08001.

[3] CMS Collaboration, "The CMS tracker system project: technical design report", Technical Report 98-006, CERN/LHCC, (1998).

[4] CMS Collaboration, "The CMS tracker: addendum to the technical design report", Technical Report 2000-016, CERN/LHCC, (2000).

[5] CMS Collaboration, "CMS Physics Technical Design Report Volume I: Detector Performance and Software", Technical Report 2006-001, CERN/LHCC, (2006).

[6] CMS Collaboration, "Commissioning and performance of the CMS silicon strip tracker with cosmic ray muons", *JINST* **5** (2010) T03008, doi:10.1088/1748-0221/5/03/T03008.

[7] CMS Collaboration, "Commissioning and performance of the CMS pixel tracker with cosmic ray muons", *JINST* **5** (2010) T03007, doi:10.1088/1748-0221/5/03/T03007.

[8] G. Flucke, P. Schleper, G. Steinbrück et al., "CMS silicon tracker alignment strategy with the Millepede II algorithm", *JINST* **3** (2008), no. 09, P09002, doi:10.1088/1748-0221/3/09/P09002.

[9] CMS Tracker Collaboration, "Alignment of the CMS silicon strip tracker during stand-alone commissioning", *JINST* **4** (2009) T07001, doi:10.1088/1748-0221/4/07/T07001.

[10] CMS Collaboration, "Commissioning of the CMS experiment and the cosmic run at four tesla", *JINST* **5** (2010) T03001, doi:10.1088/1748-0221/5/03/T03001.

[11] CMS Collaboration, "Alignment of the CMS silicon tracker during commissioning with cosmic rays", *JINST* **5** (2010) T03009, doi:10.1088/1748-0221/5/03/T03009.

[12] CMS Collaboration, "Tracking and Primary Vertex Results in First 7 TeV Collisions", *CMS Physics Analysis Summary* **CMS-PAS-TRK-10-005** (2010).

[13] CMS Collaboration, "Performance of CMS muon reconstruction in pp collision events at $\sqrt{s} = 7$ TeV", *JINST* **7** (2012) P10002, doi:10.1088/1748-0221/7/10/P10002, arXiv:1206.4071.

[14] M. French, L. Jones, Q. Morrissey et al., "Design and results from the APV25, a deep sub-micron CMOS front-end chip for the CMS tracker", *Nucl.Instrum.Meth.* **A466** (2001) 359, doi:10.1016/S0168-9002(01)00589-7.

[15] M. Raymond, R. Bainbridge, M. French et al., "Final results from the APV25 production wafer testing", in *Proceedings of the 11th Workshop on Electronics for LHC and Future Experiments (Heidelberg)*, p. 91. 2005.

[16] V. Maroussov, "Fit to an analytic form of the measured central CMS magnetic field". PhD thesis, Purdue University, 2008. CMS TS-2009/018.

[17] CMS Collaboration, "Precise mapping of the magnetic field in the CMS barrel yoke using cosmic rays", *JINST* **5** (2010) T03021, doi:10.1088/1748-0221/5/03/T03021, arXiv:0910.5530.

[18] V. Klyukhin, A. Ball, F. Bergsma et al., "Measurement of the CMS Magnetic Field", *IEEE Trans.Appl.Supercond.* **18** (2008) 295–298, doi:10.1109/TASC.2008.921242, arXiv:1110.0306.

[19] V. Blobel and C. Kleinwort, "A New Method for the High-Precision Alignment of Track Detectors", in *Conference on Advanced Statistical Techniques in Particle Physics (Durham)*. 2002. arXiv:hep-ex/0208021.

[20] V. Blobel, "Software alignment for tracking detectors", *Nucl. Instrum. Meth.* **A566** (2006) 5–13, doi:10.1016/j.nima.2006.05.157. https://www.wiki.terascale.de/index.php/Millepede_II.

[21] CMS Collaboration, "Description and Performance of the CMS Track and Primary Vertex Reconstruction", *CMS publication in preparation* **CMS-TRK-11-001** (2013).

[22] W. Hulsbergen, "The Global Covariance Matrix of Tracks Fitted with a Kalman Filter and an Application in Detector Alignment", *Nucl. Instrum. Meth.* **A600** (2009) 471, doi:10.1016/j.nima.2008.11.094, arXiv:0810.2241.

[23] V. Blobel, C. Kleinwort, and F. Meier, "Fast Alignment of a Complex Tracking Detector using Advanced Track Models", *Comp. Phys. Com.* **182** (2010) 1760, doi:10.1016/j.cpc.2011.03.017.

[24] C. Kleinwort, "General Broken Lines as Advanced Track Fitting Method", *Nucl. Instrum. Meth.* **A673** (2012) 107, doi:10.1016/j.nima.2012.01.024. https://www.wiki.terascale.de/index.php/GeneralBrokenLines.

[25] V. Blobel, "A New Fast Track-Fit Algorithm Based on Broken Lines", *Nucl. Instrum. Meth.* **A566** (2006), no. 1, 14, doi:10.1016/j.nima.2006.05.156.

[26] A. Strandlie and W. Wittek, "Derivation of Jacobians for the propagation of the covariance matrices of track parameters in homogeneous magnetic fields", *Nucl. Instr. Methods Phys. Res.* **A566** (2006) 687. CMS-NOTE-2006-001.

[27] V. Karimäki, A. Heikkinen, T. Lampén et al., "Sensor Alignment by Tracks", *eConf* **C0303241** (2003) TULT008, arXiv:physics/0306034.

[28] D. N. Brown, A. V. Gritsan, Z. J. Guo, and D. A. Roberts, "Local alignment of the BABAR silicon vertex tracker", *Nucl. Instrum. Meth.* **A603** (2009) 467–484, doi:10.1016/j.nima.2009.02.001.

[29] J. Draeger, "Track Based Alignment of the CMS Silicon Tracker and its Implication on Physics Performance". PhD thesis, Universität Hamburg, 2011.

[30] E. Widl and R. Frühwirth, "Representation and Estimation of Trajectories from Two-body Decays", *CMS Note* **2007/032** (2007).

[31] CMS Collaboration, "Measurements of Inclusive W and Z Cross Sections in pp Collisions at $\sqrt{s} = 7$ TeV", *J. High Energy Phys.* **01** (2011) 080, doi:10.1007/JHEP01(2011)080.

[32] CMS Collaboration, "Measurement of the Rapidity and Transverse Momentum Distributions of Z Bosons in pp Collisions at $\sqrt{s} = 7$ TeV", *Phys. Rev.* **D85** (2012) 032002, doi:10.1103/PhysRevD.85.032002.

[33] The ALEPH, DELPHI, L3, OPAL, SLD Collaborations, the LEP Electroweak Working Group, the SLD Electroweak and Heavy Flavour Groups, "Precision Electroweak Measurements on the Z Resonance", *Phys. Rept.* **427** (2006) 257, arXiv:hep-ex/0509008.

[34] C. Paige and M. Saunders, "Solution of Sparse Indefinite Systems of Linear Equations", *SIAM Journal on Numerical Analysis* **12** (1975), no. 4, 617.

[35] OpenMP®. http://openmp.org.

[36] M. Swartz et al., "A new technique for the reconstruction, validation and simulation of hits in the CMS pixel detector", *PoS Vertex 2007* (2007) 035.

[37] CMS Collaboration, "Identification of b-quark jets with the CMS experiment", *JINST* **8** (2013) P04013, doi:10.1088/1748-0221/8/04/P04013, arXiv:1211.4462.

[38] B. Wittmer, R. Adolphi, M. Henke et al., "The laser alignment system for the CMS silicon microstrip tracker", *Nucl.Instrum.Meth.* **A581** (2007) 351–355, doi:10.1016/j.nima.2007.08.002.

[39] R. Frühwirth, W. Waltenberger, and P. Vanlaer, "Adaptive Vertex Fitting", *CMS Note* **2007/008** (2007).

[40] H. Enderle, "Momentum bias determination in the tracker alignment and first differential $t\bar{t}$ cross section measurement at CMS". PhD thesis, Universität Hamburg, 2012.